Charge-changing cross sections for $^{42–51}$Ca and effect of charged-particle evaporation induced by neutron-removal reactions

M. Tanaka,[1,2,*] M. Takechi,[3] A. Homma,[3] A. Prochazka,[4] M. Fukuda,[2] D. Nishimura,[5] T. Suzuki,[6] T. Moriguchi,[7] D. S. Ahn,[1] A. Aimaganbetov,[8,9] M. Amano,[7] H. Arakawa,[6] S. Bagchi,[4,10,11,†] K.-H. Behr,[4] N. Burtebayev,[8,12] K. Chikaato,[3] H. Du,[2] T. Fujii,[6] N. Fukuda,[1] H. Geissel,[4] T. Hori,[2] S. Hoshino,[3] R. Igosawa,[6] A. Ikeda,[3] N. Inabe,[1] K. Inomata,[6] K. Itahashi,[1] T. Izumikawa,[13] D. Kamioka,[7] N. Kanda,[3] I. Kato,[6] I. Kenzhina,[8,12] Z. Korkulu,[14,1] Y. Kuk,[8,9] K. Kusaka,[1] K. Matsuta,[2] M. Mihara,[2] E. Miyata,[3] D. Nagae,[1,15] S. Nakamura,[2] M. Nassurlla,[8,12] K. Nishimuro,[6] K. Nishizuka,[3] K. Ohnishi,[2] M. Ohtake,[1] T. Ohtsubo,[3] S. Omika,[6] H. J. Ong,[16] A. Ozawa,[7] H. Sakurai,[1,17] C. Scheidenberger,[4] Y. Shimizu,[1] T. Sugihara,[2] T. Sumikama,[1] H. Suzuki,[1] S. Suzuki,[7] H. Takeda,[1] Y. Tanaka,[2] Y. K. Tanaka,[4] I. Tanihata,[16,18] T. Wada,[3] K. Wakayama,[6] S. Yagi,[2] T. Yamaguchi,[6] R. Yanagihara,[2] Y. Yanagisawa,[1] K. Yoshida,[1] and T. K. Zholdybayev[8,12]

[1] *RIKEN Nishina Center, Wako, Saitama 351-0198, Japan*
[2] *Department of Physics, Osaka University, Toyonaka, Osaka 560-0043, Japan*
[3] *Department of Physics, Niigata University, Ikarashi, Niigata 951-2181, Japan*
[4] *GSI Helmholtzzentrum für Schwerionenforschung, 64291 Darmstadt, Germany*
[5] *Department of Physics, Tokyo City University, Setagaya, Tokyo 158-8557, Japan*
[6] *Department of Physics, Saitama University, Saitama 338-8570, Japan*
[7] *Institute of Physics, University of Tsukuba, Tsukuba, Ibaraki 305-8571, Japan*
[8] *Institute of Nuclear Physics, 050032 Almaty, Kazakhstan*
[9] *L.N. Gumilyov Eurasian National University, 010008 Astana, Kazakhstan*
[10] *Astronomy and Physics Department, Saint Mary's University, Halifax, Nova Scotia B3H 3C3, Canada*
[11] *Justus Liebig University, 35392 Giessen, Germany*
[12] *Al-Farabi Kazakh National University, 050040 Almaty, Kazakhstan*
[13] *Institute for Research Promotion, Niigata University, Niigata 950-8510, Japan*
[14] *Center for Exotic Nuclear Studies, Institute for Basic Science, Daejeon 34126, Republic of Korea*
[15] *Research Center for Superheavy Elements, Kyushu University, Fukuoka 819-0395, Japan*
[16] *Research Center for Nuclear Physics, Osaka University, Ibaraki, Osaka 567-0047, Japan*
[17] *Department of Physics, University of Tokyo, Bunkyo-ku, Tokyo 113-0033, Japan*
[18] *School of Physics and Nuclear Energy Engineering, Beihang University, 100191 Beijing, China*

(Received 26 November 2021; revised 23 June 2022; accepted 8 July 2022; published 25 July 2022)

Charge-changing cross sections σ_{CC} for $^{42–51}$Ca on a carbon target at around 280 MeV/nucleon have been measured. Though the existing point-proton radii r_{p} of Ca isotopes increase as the neutron number increases, the measured σ_{CC} data show a significant decrease, which is against the expectation from a simple Glauber-like model. We found that this observed phenomenon could be attributed to the charged-particle evaporation effect induced by the neutron-removal reaction. By taking the evaporation effect into account, various σ_{CC} data sets for nuclides from C to Fe isotopes on ^{12}C measured at around 280 MeV/nucleon are reproduced with a standard deviation of 1.6%. It is also clarified that this evaporation effect becomes negligibly small in the neutron-rich region. The evaluated relation between σ_{CC} and r_{p} using the current model indicates that σ_{CC} data for neutron-rich Ca isotopes ($A \geqslant 51$) are highly sensitive to r_{p}. This high sensitivity potentially allows one to determine the r_{p} of very neutron-rich nuclei.

DOI: 10.1103/PhysRevC.106.014617

I. INTRODUCTION

The point-proton radius r_{p} of the atomic nucleus, usually defined as the root mean square (RMS) radius of the point-proton density distribution, is one of the key quantities used to study nuclear structures. Point-proton or charge radii have been measured using the electron elastic scattering, muonic x-ray, and optical isotope shift (IS) methods [1]. Among these, the IS measurement is generally regarded as the only way to extract the r_{p} of unstable nuclei. Systematic r_{p} investigations have helped clarify exotic phenomena, such as the neutron-halo structure [2,3] and the dramatic enhancement of nuclear radii beyond the magic numbers [4,5]. The neutron-skin thickness can be also extracted from r_{p} combined with the matter radius r_{m} [6,7]. The pursuit of neutron-skin thickness has

---

[*] masaomi.tanaka@riken.jp

[†] Present address: Indian Institute of Technology (Indian School of Mines) Dhanbad, Jharkhand 826004, India.

attracted significant attention particularly for very neutron-rich nuclei, to elucidate the density-dependent parameter of the symmetry energy term in the nuclear-matter equation of state [8]. However, the IS method is inapplicable to unstable nuclei far from the stability line, or certain elements, because of beam production difficulties.

Alternative r_p determination methods for unstable nuclei have been proposed, based on reaction cross sections on proton and carbon targets [9–11], proton elastic scattering at double energies [12], and electron elastic scattering under trapping in a storage ring [13–15]. The charge-changing cross section σ_{CC}, defined as the atomic-number-changing total cross section, can potentially also be used to derive r_p. Similarly to the interaction cross section σ_I or reaction cross section σ_R, which are sensitive to r_m, σ_{CC} is used to probe r_p [16,17]. Furthermore, σ_{CC} can be measured even with low-intensity heavy-ion beams [e.g., a few particles per second (pps)]. Therefore, this method is a potential tool to study the r_p of a very neutron-rich nucleus.

To date, σ_{CC} measurement has been utilized to derive the r_p of light-mass nuclei [18–30]. Several methods based on the Glauber model have been proposed to describe the relationship between σ_{CC} and r_p. For example, Yamaguchi *et al.* previously introduced an empirical scaling factor for the Glauber-like model to explain experimental σ_{CC} data for ^{28}Si on a carbon target at intermediate energies of 100–600 MeV/nucleon [18]. This phenomenological model universally explained σ_{CC} data at 300 MeV/nucleon for light-mass nuclei over a wide range of mass-to-atomic-number ratios A/Z [19]. However, some σ_{CC} data for medium-mass nuclides around calcium deviate from the above phenomenological-model calculation [20,21]. A similar approach introducing an empirical parameter has been proposed in another study [31]. In contrast, σ_{CC} data for nuclei up to nitrogen at ≈ 900 MeV/nucleon have been explained by a Glauber-like calculation without the above scaling factor [24–27]. To explain σ_{CC} for ^{12}C on ^{12}C at 10–2100 MeV/nucleon, Tran *et al.* tuned the slope parameter of the proton-neutron elastic differential cross section, β_{ij}, which is one of the parameters in the Glauber-model calculation [28]. However, their model underestimated the σ_{CC} data for ^{12}C on ^{12}C at 200–400 MeV/nucleon. Although theoretical studies have investigated this problem [32,33], a consistent universal model for r_p derivation from σ_{CC} has not been established. The mechanism underlying the discrepancy between the experimental data and the Glauber model remains crucially unknown.

In this study, we report measurement of σ_{CC} on a carbon target at around 280 MeV/nucleon for $^{42-51}$Ca, for which r_p was previously measured via the IS method [4]. The obtained σ_{CC} results show a significant decrease with increases in the neutron number, a trend that differs from those in light-mass isotopic chains. Based on a comparison between the experimental results and the calculations of the Glauber-like model (taking the known r_p as input values), the reaction dynamics in the charge-changing process were investigated. The Glauber-like model could not explain the trends of experimental σ_{CC} values. On the other hand, the calculation which takes into account the charged-particle evaporation effect induced by the neutron-removal reactions explains the decrease of σ_{CC} against the increment of neutron number very well. This model systematically reproduces σ_{CC} data for various nuclides from C to Fe isotopes measured at around 280 MeV/nucleon without any empirical corrections.

TABLE I. Measured charge-changing cross sections σ_{CC} for $^{42-51}$Ca on ^{12}C target. The categories of nuclides measured simultaneously are listed in the second column. The mean energies in the reaction target are listed in the third column. The first and second parentheses in the fourth column contain the statistical and systematic uncertainties, respectively.

Nuclide	Category	E_{mean} (MeV/nucleon)	σ_{CC} (mb)
^{42}Ca	Run1	297	1378(11)(6)
^{43}Ca	Run1	284	1352(9)(7)
^{44}Ca	Run1	270	1351(10)(10)
^{45}Ca	Run2	302	1291(6)(10)
^{46}Ca	Run2	290	1300(8)(15)
^{47}Ca	Run2	277	1283(14)(14)
^{48}Ca	Run3	300	1259(14)(16)
^{49}Ca	Run3	291	1280(8)(18)
^{50}Ca	Run3	283	1297(11)(23)
^{51}Ca	Run3	271	1319(33)(28)

II. EXPERIMENT AND ANALYSIS

A. Experiment

The experiment was conducted at the RI Beam Factory (RIBF), operated by the RIKEN Nishina Center, and the Center for Nuclear Study, University of Tokyo. A 345-MeV/nucleon ^{238}U primary beam and a rotating beryllium production target were used to produce $^{42-51}$Ca secondary beams. The secondary beams produced at the F0 focal plane were roughly purified in the first stage of the BigRIPS fragment separator [34] between the F0 and F3 focal planes. Then, σ_{CC} was measured between the F3 and F7 focal planes. Owing to the large acceptance of BigRIPS, experimental data were acquired for three or four Ca isotopes simultaneously in a single BigRIPS setting. The groups of simultaneously measured nuclides and σ_{CC} results of them are listed in the second column of Table I.

The transmission method was applied to measure σ_{CC} [35], where

$$\sigma_{CC} = -\frac{1}{N_t}\ln\left(\frac{\gamma}{\gamma_0}\right), \tag{1}$$

with N_t being the number of target nuclei per unit area and γ and γ_0 the nonreaction rates with and without the reaction target, respectively. Note that, for σ_{CC} measurement, outgoing particles with the same Z as the incoming ones correspond to the nonreaction events. A wedge-shaped carbon target with an angle of 9.61 mrad was placed at the F5 momentum-dispersive focal plane to maintain the achromatic property of the F7 focal plane. The central-point thickness of the target was 1.803(3) g/cm^2. The σ_{CC} value with the wedge-shaped target was obtained from the values at each position, i.e., $\sigma_{CC}(X)$, weighted with the incident-particle distri-

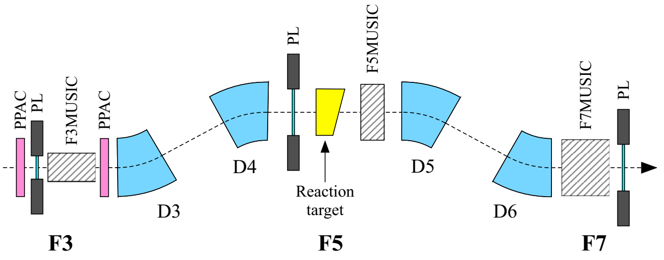

FIG. 1. Schematic view of the experimental setup.

bution on the target, $N_{\rm in}(X)$, where X is the position along the momentum-dispersive (horizontal) direction perpendicular to the beam axis z. The target-thickness profile $d(X)$ was measured with 0.15% accuracy or higher. The mean energies in the reaction target, $E_{\rm mean}$, at the weighted mean position of $N_{\rm in}(X)$ are listed in Table I. The average $E_{\rm mean}$ of the $^{42\text{–}51}$Ca data was approximately 280 MeV/nucleon. Note that the experimental $\sigma_{\rm CC}$ data reported herein were obtained simultaneously with $\sigma_{\rm I}$ data for $^{42\text{–}51}$Ca [7]. Figure 1 shows the experimental setup between the F3 and F7 focal planes of BigRIPS. To derive the nonreaction rate, the incoming and nonreacting outgoing particles were counted before and after the reaction target, respectively. For particle identification (PID) before the reaction target, the mass-to-charge ratio A/Q and Z of the incoming particle were identified in event-by-event mode via the $B\rho$-TOF-ΔE method between the F3 and F5 focal planes, where $B\rho$, TOF, and ΔE represent the magnetic rigidity, time of flight, and energy loss, respectively. Here, $B\rho$ was determined from the dipole-magnet magnetic field data together with the beam-ray tracking using parallel plate avalanche counters (PPACs) at F3 and a plastic scintillation counter (PL) at F5, which was sensitive to X. The TOF was measured by PLs installed at F3 and F5. A multisampling ionization chamber (MUSIC) at F3 (F3MUSIC) was used to measure ΔE.

In the downstream side of the reaction target, i.e., between F5 and F7, Z was identified from the ΔE measured by two MUSICs installed at F5 and F7 (F5MUSIC and F7MUSIC, respectively). F5MUSIC is a large acceptance specification (240 mm × 150 mm area and 200 mm length), whereas F7MUSIC is a high resolution specification (240 mm ϕ area and 480 mm length). Between the F5 and F7 focal planes, BigRIPS was tuned to transport particles that changed neither A nor Z at the reaction target. Therefore, only non-nuclide-changing and one-neutron-removal events of Ca isotopes [^{42}Ca and ^{41}Ca in Fig. 2(b)] were transported to the F7 focal plane, owing to the ±3% momentum acceptance of BigRIPS. The Z resolution of F7MUSIC was much higher than that of F5MUSIC. For clear identification and reliable counting of the nonreacting particles, the non-nuclide-changing and one-neutron-removal particles of Ca isotopes were identified by using F7MUSIC. The other Ca-isotope particles were identified from the ΔE data of F5MUSIC only. To ensure the full acceptance of nonreacting particles after the reaction target, the position, angle, and momentum information from upstream detectors was constrained. This constraint was optimized for nuclides of interest.

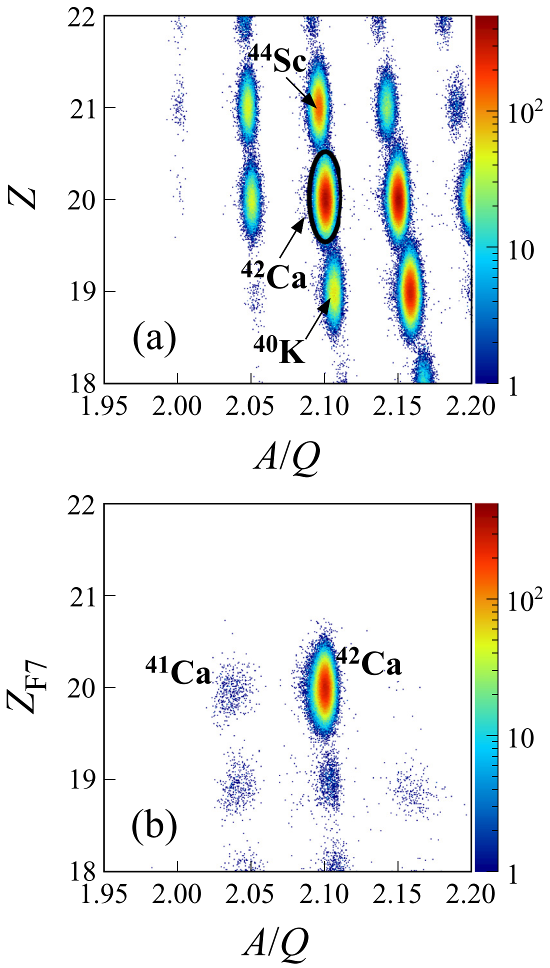

FIG. 2. Particle-identification plots of (a) the cocktail beam for the ^{42}Ca setting before the reaction target and (b) particles transported to the F7 focal plane, with incoming ^{42}Ca selection indicated by the ellipse in (a). In (b), Z was determined from F7MUSIC ΔE. The appropriate beam-emittance constraint was adopted for both plots. The ^{48}Ca plots are presented in Ref. [7].

B. Data analysis and results

Figure 2(a) shows the typical PID plot for the beam before the reaction target for ^{42}Ca, as an example. The nuclides were separated with 19.2σ and 6.5σ resolutions on A/Q and Z, respectively. The ^{42}Ca incident particles were selected by an elliptical gate with a width of 3.5σ of each axis. Contamination from neighboring nuclides, i.e., ^{44}Sc and ^{40}K, was excluded through additional selection in the correlation between the ΔE in F3MUSIC and those in the F3 and F5 PLs. Finally, these contaminants had effects far lower than 0.1% on $\sigma_{\rm CC}$.

Figure 3 shows the Z identification plot for the incoming Ca isotopes after the reaction target. The events transported to the F7 focal plane were identified from the correlation plot between the atomic numbers determined by F5MUSIC and F7MUSIC, i.e., $Z_{\rm F5}$ and $Z_{\rm F7}$, respectively [Fig. 3(a)]. The peak separations of $Z_{\rm F5}$ and $Z_{\rm F7}$ were 3.0σ and 6.3σ, respectively. The events within the black lines in Fig. 3(a) were counted as nonreacting particles. Here, the widths of elliptical

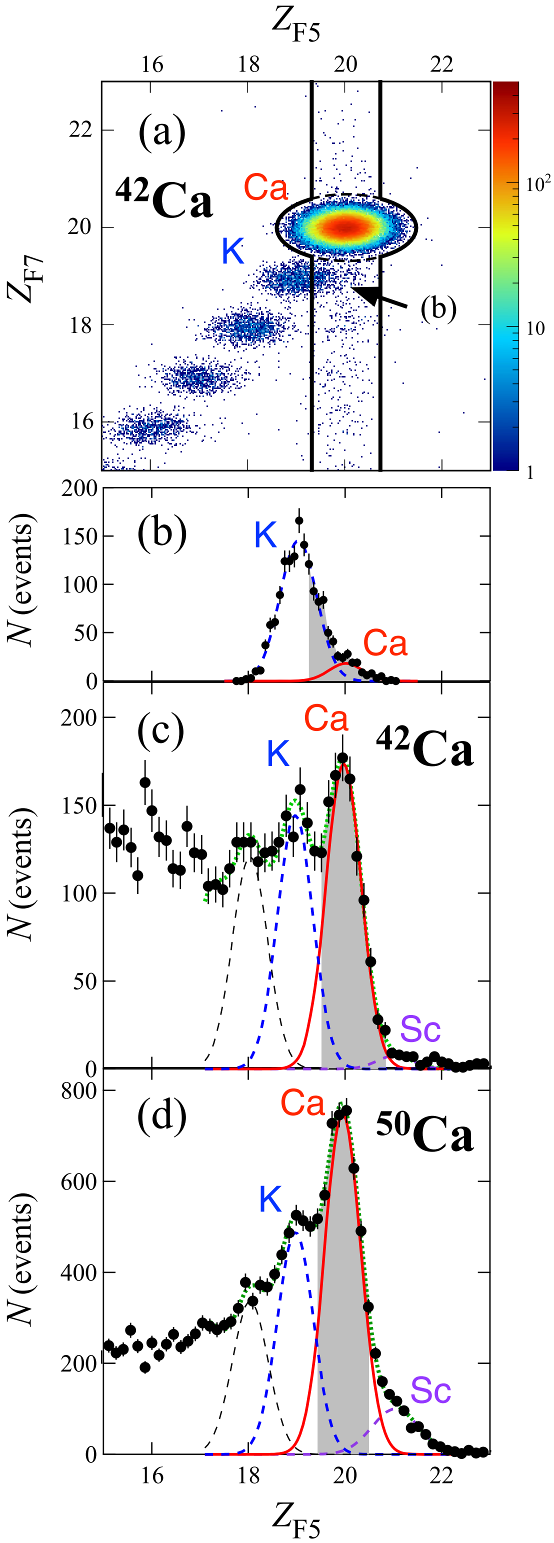

FIG. 3. (a) Identification of Z after the reaction target with selection of incoming ^{42}Ca in correlation between Z_{F5} and Z_{F7}. The events inside the black lines were counted. (b) Z_{F5} histogram for $Z_{F7} = 19$ events indicated by the arrow in plot (a). The shaded region corresponds to the area enclosed by the black line in plot (a). (c,d) Z_{F5} histograms for events that were not transported to F7 in cases of ^{42}Ca and ^{50}Ca, respectively. The dotted green line represents the fitting result. The red solid and dashed lines indicate the compositions.

and vertical-lines regions are 4σ and 2σ, respectively. The K-isotope contaminants indicated by the arrow were subtracted by fitting the Z_{F5} histogram shown in Fig. 3(b). The particles that were not transported to F7 were identified in the Z_{F5} histograms shown in Figs. 3(c) and 3(d). Although the Z_{F5} resolution was insufficient for complete peak separation, fitting was achieved with the help of Z_{F7}. In this fit, the position and width of each element in Z_{F5} were constrained using data on the peaks tagged by Z_{F7} in Fig. 3(a). The events in the shaded areas, where the Ca events are dominant, were regarded as nonreacting particles. The Ca events outside this region and neighboring-element contaminants were corrected based on the fitted distributions [the red solid and dashed lines in Figs. 3(c) and 3(d)]. This event-counting uncertainty in the identification only on Z_{F5} was typically 7%. The ratio of the number of nonreaction events identified in Figs. 3(c) and 3(d), N_{F5}, to that identified in Fig. 3(a), N_{F7}, was larger for a neutron-rich nucleus. For example, the N_{F5}/N_{F7} values for ^{42}Ca and ^{50}Ca were 0.0079(4) and 0.0285(20), respectively.

The experimental data without the reaction target for the respective isotopes were similarly analyzed. For example, γ and γ_0 of ^{42}Ca were 0.8744(8) and 0.9914(4), respectively. Table I summarizes the obtained σ_{CC} for $^{42\text{–}51}$Ca on ^{12}C. The statistical uncertainties (first parentheses) were typically less than 1.0%. The main source of systematic uncertainty (second parentheses) was the accuracy of N_{F5}. As mentioned above, N_{F5}/N_{F7} increases with increases in the neutron number of the nuclide of interest. Therefore, the total uncertainty is governed by a systematic uncertainty, especially in neutron-rich isotopes. Below, we treat the square root of the sum of these two uncertainties as the total uncertainty.

III. DISCUSSION

Figure 4(b) shows the present σ_{CC} results for Ca isotopes as a function of mass number A. The existing data are also shown for comparison [20,21]. The minimum energy of the present study and the energy of existing data were $E = 270$ and 300 MeV/nucleon, respectively. A negligibly small difference of 0.2% in σ_{CC} due to its energy dependence was estimated between these energies. Therefore, this slight difference was ignored and the calculation was performed for 280 MeV/nucleon. The present and existing data [20,21] are consistent for ^{42}Ca and ^{45}Ca, but not for ^{44}Ca and ^{46}Ca. However, the present σ_{CC} results of Ca isotopes show a decreasing trend similar to the existing data of Ca, Ti, Cr, and Fe isotopes [20,21], which will be mentioned later in Fig. 6. Upon extension of the experimental data to the neutron-rich region, σ_{CC} decreased with increasing mass or neutron number. On the other hand, this A dependence of Ca isotopes significantly differs from the experimental σ_{CC} trend in the light-mass region [17,24–28], which shows rather flat dependence on A. To understand the trend of the experimental σ_{CC} of Ca isotopes, we first performed the Glauber-like calculation.

A. Glauber-like model

As indicated in the Introduction, the σ_{CC} data for deriving r_p are usually discussed based on the Glauber-like calculation

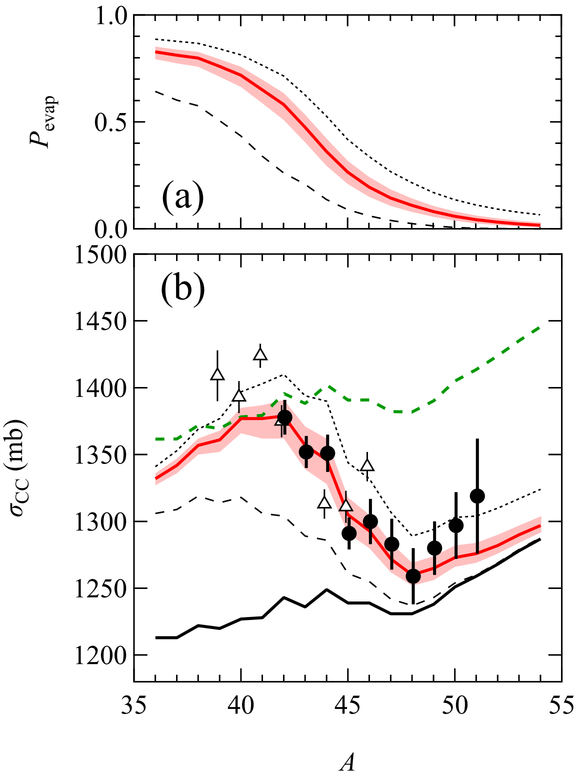

FIG. 4. (a) A dependence of P_{evap} values [Eq. (18)] with $E_{\max} =$ 20 MeV (thin black dashed line), 45(8) MeV (red solid line), and 70 MeV (thin black dotted line). (b) A dependence of σ_{CC} for Ca isotopes on ^{12}C. The present $^{42-51}$Ca results and existing data [20,21] are indicated by closed circles and open triangles, respectively. The black solid line and green dashed line represent the σ_{CC} values from the Glauber(ZROLA) calculation [Eq. (12)] and the Glauber-like(ZROLA) calculation with the correction factor [18] (Eq. (13)), respectively. The thin black dashed line, red solid line, and thin black dotted line show the σ_{CC} calculations from the Glauber(CE) model [Eq. (17)] with $E_{\max} =$ 20, 45(8), and 70 MeV, respectively.

[18–31,33]. There are several types of Glauber model calculations for σ_{R} and σ_{CC} that incorporate various effects such as multiple scattering [36], energy-dependent range parameters [28,37], and Fermi motion [38].

Here, to describe both the σ_{R} and σ_{CC} in the same framework, we implemented the zero range optical limit approximation (ZROLA) with a nucleon–nucleon (NN) total cross section that takes the Fermi motion effect into account. The Fermi motion effect was introduced into the Glauber-model calculation in almost the same way as in Ref. [38]. As shown in Figs. 4 and 5, which will be discussed later, the applied Glauber model can reproduce the experimental values of both σ_{R} and σ_{CC} simultaneously and consistently. Furthermore, this model can reproduce the energy dependences of σ_{R} for ^{9}Be and ^{27}Al on ^{12}C (Appendix A), and that of σ_{CC} for ^{28}Si on ^{12}Ca at $E > 200$ MeV/nucleon shown in Fig. 14 (to be mentioned later). It should also be mentioned that the introduction of the Fermi motion itself does not influence the essence of the following discussion concerning σ_{CC} measured at 280 MeV/nucleon (see Appendix B).

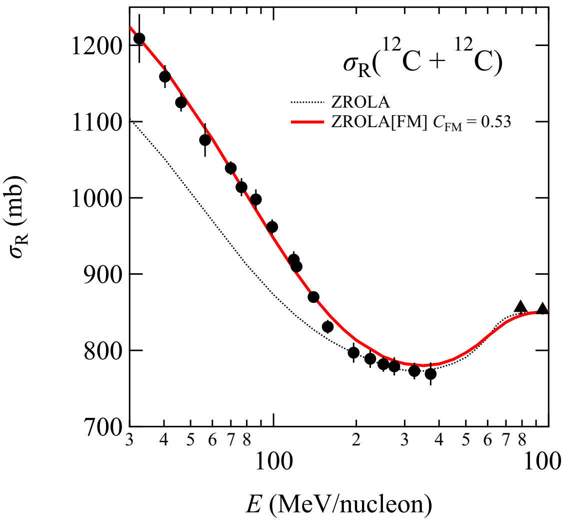

FIG. 5. Energy dependence of σ_{R} for ^{12}C on ^{12}C [16,38,39]. The red solid and black dotted lines indicate the present ZROLA calculation with the best-fit parameter for the Fermi motion, $C_{\mathrm{FM}} = 0.53$, and the conventional ZROLA calculation without the Fermi motion effect on σ_{ij}, respectively.

In this framework, σ_{R} is expressed using the transmission function $T(b)$ as follows:

$$\sigma_{\mathrm{R}} = 2\pi \int b[1 - T(b)]db, \tag{2}$$

$$T(b) \equiv \exp\left[- \int ds \left(\sum_{i,j} \sigma_{ij}(\boldsymbol{b}, \boldsymbol{s})\, \overline{\rho}_i^{\mathrm{P}}(s) \overline{\rho}_j^{\mathrm{T}}(|\boldsymbol{b} - \boldsymbol{s}|) \right) \right], \tag{3}$$

where b is an impact parameter; s and $|\boldsymbol{b} - \boldsymbol{s}|$ are the distances from the centers of the projectile and target nuclei, respectively; the indexes i, j denote the isospins of the nucleons in projectile and target nuclei, respectively; σ_{ij} is the NN total cross section; and $\overline{\rho}^{\mathrm{P}}(r)$ and $\overline{\rho}^{\mathrm{T}}(r)$ are density distributions of the projectile and target integrated along beam axis z, i.e., $\overline{\rho}(\boldsymbol{b}) = \int \rho(\boldsymbol{b}, z)dz$, respectively.

We applied the effective NN cross section ($\sigma_{\mathrm{NN}}^{\mathrm{eff}}$) that includes the Fermi motion effect of the nucleons in the nucleus [38]. Here, $\sigma_{\mathrm{NN}}^{\mathrm{eff}}$ was calculated from the bare NN cross section ($\sigma_{\mathrm{NN}}^{\mathrm{bare}}$) averaged by the distribution of the relative momentum (p_{rel}) of the colliding nucleons in the projectile and target nuclei, $D(p_{\mathrm{rel}})$:

$$\sigma_{ij}^{\mathrm{eff}}(\boldsymbol{b}, \boldsymbol{s}) = \int_{-\infty}^{\infty} dp_{\mathrm{rel}} \sigma_{ij}^{\mathrm{bare}}(p_{\mathrm{rel}}) D_{ij}(p_{\mathrm{rel}}, \boldsymbol{b}, \boldsymbol{s}), \tag{4}$$

$$D_{ij}(p_{\mathrm{rel}}, \boldsymbol{b}, \boldsymbol{s}) = \frac{1}{\sqrt{2\pi\left[\langle p^2\rangle_i^{\mathrm{P}}(s) + \langle p^2\rangle_j^{\mathrm{T}}(|\boldsymbol{b} - \boldsymbol{s}|)\right]}} \times \exp\left[-\frac{(p_{\mathrm{rel}} - p_{\mathrm{P}})^2}{2\left(\langle p^2\rangle_i^{\mathrm{P}}(s) + \langle p^2\rangle_j^{\mathrm{T}}(|\boldsymbol{b} - \boldsymbol{s}|)\right)} \right], \tag{5}$$

where $\langle p^2\rangle^{\mathrm{P}}$ and $\langle p^2\rangle^{\mathrm{T}}$ are the mean-square momenta of the nucleon in the projectile and target nuclei, respectively, and p_{P} is the momentum of the entire projectile nucleus. In Ref. [38], a fixed value of 90 MeV/c was generally adopted as the value of $\langle p^2\rangle^{1/2}$ based on the Goldhaber model [40], while here the $\langle p^2\rangle^{1/2}$ was calculated from the density-dependent Fermi momentum averaged along z:

$$p_{\mathrm{Fermi},i}(s,z) = \hbar[3\pi^2\rho_i(s,z)]^{1/3}, \tag{6}$$

$$p^z_{\mathrm{Fermi},i}(s) = \frac{\int p_{\mathrm{Fermi},i}(s,z)\rho_i(\sqrt{s^2+z^2})dz}{\int \rho_i(\sqrt{s^2+z^2})dz}, \tag{7}$$

$$[\langle p^2\rangle_i(s)]^{1/2} = C_{\mathrm{FM}}\, p^z_{\mathrm{Fermi},i}(s). \tag{8}$$

Here, C_{FM} is a constant parameter, which was set to 0.53 to reproduce the energy dependence of experimental σ_{R} data for ^{12}C on ^{12}C [16,38,39] (Fig. 5). The point-proton and point-neutron density distributions $\rho_{\mathrm{p}}(r)$ and $\rho_{\mathrm{n}}(r)$, respectively, introduced in Ref. [38], were used as the density profile of ^{12}C. Note that $C_{\mathrm{FM}} = 0.53$ is roughly consistent with the Goldhaber model ($C_{\mathrm{FM}} = 0.45$ derived from Eqs. (5) and (6) of Ref. [40]). The small deviation from the Goldhaber's value may be due to the fact that the consideration of the Fermi-motion effect effectively includes other effects that are not considered in the present calculation such as the multiple scattering and energy-dependent range parameters [28,37,38]. Note that the calculation with $C_{\mathrm{FM}} = 0.45$ still reproduces the experimental data in Fig. 5 within 1.5% deviation in the energy range of $E > 150$ MeV/nucleon.

In analogy with the Glauber model for σ_{R}, σ_{CC} is usually formulated by ignoring the contribution of the neutrons in the projectile nucleus. Here, $T(b)$ can be explicitly written according to the projectile composition [31]:

$$T(b) = T_{\mathrm{p}}(b)T_{\mathrm{n}}(b), \tag{9}$$

$$T_{\mathrm{p}}(b) = \exp\left[-\int ds\bar{\rho}^{\mathrm{P}}_{\mathrm{p}}\{\sigma_{\mathrm{pp}}\bar{\rho}^{\mathrm{T}}_{\mathrm{p}} + \sigma_{\mathrm{pn}}\bar{\rho}^{\mathrm{T}}_{\mathrm{n}}\}\right], \tag{10}$$

$$T_{\mathrm{n}}(b) = \exp\left[-\int ds\bar{\rho}^{\mathrm{P}}_{\mathrm{n}}\{\sigma_{\mathrm{np}}\bar{\rho}^{\mathrm{T}}_{\mathrm{p}} + \sigma_{\mathrm{nn}}\bar{\rho}^{\mathrm{T}}_{\mathrm{n}}\}\right]. \tag{11}$$

Then, the charge-changing cross section is obtained as

$$\tilde{\sigma}_{\mathrm{CC}} = 2\pi\int b[1-T_{\mathrm{p}}(b)]db. \tag{12}$$

Here, we denote this quantity as $\tilde{\sigma}_{\mathrm{CC}}$. In this Glauber-like calculation, only $\rho_{\mathrm{p}}(r)$ in the projectile nucleus is assumed to contribute to the charge-changing cross section. Based on Eq. (12), in the empirical method [18], σ_{CC} is expressed by introducing the energy-dependent scaling factor $\varepsilon(E)$:

$$\sigma_{\mathrm{CC}} = \varepsilon(E)\tilde{\sigma}_{\mathrm{CC}}. \tag{13}$$

At $E = 280$ MeV/nucleon, $\varepsilon = 1.123$.

For the Glauber-model calculation, we assumed the two-parameter Fermi-type (2pF) function for $\rho_{\mathrm{p}}(r)$ of Ca isotopes:

$$\rho_{\mathrm{p}}(r) = \frac{\rho_{\mathrm{p0}}}{1+\exp\left(\frac{r-C_{\mathrm{p}}}{a_{\mathrm{p}}}\right)}, \tag{14}$$

TABLE II. The r_{p} values of Ca isotopes used in the calculation deduced from the experimental data of charge radii [1,4,43].

Nuclide	r_{p} (fm)	Nuclide	r_{p} (fm)
^{36}Ca	3.345	^{46}Ca	3.401
^{37}Ca	3.345	^{47}Ca	3.384
^{38}Ca	3.364	^{48}Ca	3.384
^{39}Ca	3.361	^{49}Ca	3.399
^{40}Ca	3.377	^{50}Ca	3.428
^{41}Ca	3.379	^{51}Ca	3.444
^{42}Ca	3.411	^{52}Ca	3.465
^{43}Ca	3.397	^{53}Ca	3.487
^{44}Ca	3.423	^{54}Ca	3.508
^{45}Ca	3.400		

where ρ_{p0}, C_{p}, and a_{p} are the density constant, half-density radius, and diffuseness, respectively. We assumed that the central density $\rho_{\mathrm{p}}(0) = \rho_{\mathrm{p0}}/[1+\exp(-C_{\mathrm{p}}/a_{\mathrm{p}})]$ was 0.088 fm^{-3}, i.e., half that of the central density of the nucleon density distribution adopted in Ref. [7]. The remaining two parameters were determined to satisfy the known r_{p} and the volume integral $Z = \int \rho_{\mathrm{p}}(r)d^3r$. The r_{p} was obtained from the RMS charge radius r_{ch} as follows:

$$r_{\mathrm{p}}^2 = r_{\mathrm{ch}}^2 - R_{\mathrm{p}}^2 - \frac{N}{Z}R_{\mathrm{n}}^2 - \frac{3\hbar^2}{4m_{\mathrm{p}}^2c^2}, \tag{15}$$

where R_{p} and R_{n} are the RMS charge radii of the proton and neutron, respectively, and the last term is the Darwin–Foldy term [41,42]. Table II summarizes the r_{p} values obtained from r_{ch} through Eq. (15). The existing r_{ch} data [1,4,43] were used for $^{36\text{–}52}$Ca, while the r_{p} values for ^{53,54}Ca were extrapolated from those for $^{48\text{–}52}$Ca. This is because r_{p} increases linearly in all isotopic chains beyond $N = 28$ [44].

In Fig. 4(b), the values calculated using Eqs. (12) and (13) are indicated by black solid and green dashed lines, respectively. Although both calculations failed to reproduce the A dependence of experimental data, each worked well in a particular region: $\tilde{\sigma}_{\mathrm{CC}}$ [Eq. (12)] was closer to the experimental values in the neutron-rich region, but the calculation using the correction factor [Eq. (13)] effectively reproduced the experimental σ_{CC} of the stable nucleus around ^{42}Ca. This can be attributed to the determination of $\varepsilon(E)$ from the experimental σ_{CC} for the stable nucleus, ^{28}Si [18]. Thus, to explain the overall trend of experimental data, mechanisms other than the conventional Glauber model are required. The ratios of experimental σ_{CC} values to the calculated $\tilde{\sigma}_{\mathrm{CC}}$ values using Eq. (12) are indicated as a function of one-proton separation energy S_{p} in Fig. 6. The S_{p} values were obtained from Ref. [45]. In addition to the present results of $^{42\text{–}51}$Ca, the existing σ_{CC} data of Ca, Ti, Cr, and Fe isotopes [20,21] are also plotted by the open triangles. Here, the 2pF functions were assumed for $\rho_{\mathrm{p}}(r)$ in Ti, Cr, and Fe isotopes to calculate $\tilde{\sigma}_{\mathrm{CC}}$. The parameters of $\rho_{\mathrm{p}}(r)$ were determined in the same manner as the Ca isotopes using the known r_{p} values [1], except for ^{55,59,60}Fe. The r_{p} values for ^{55,59,60}Fe were estimated from experimental r_{p} of $^{54,56\text{–}58}$Fe [1]. It can be seen that the data for various nuclei commonly deviate more from the Glauber-like

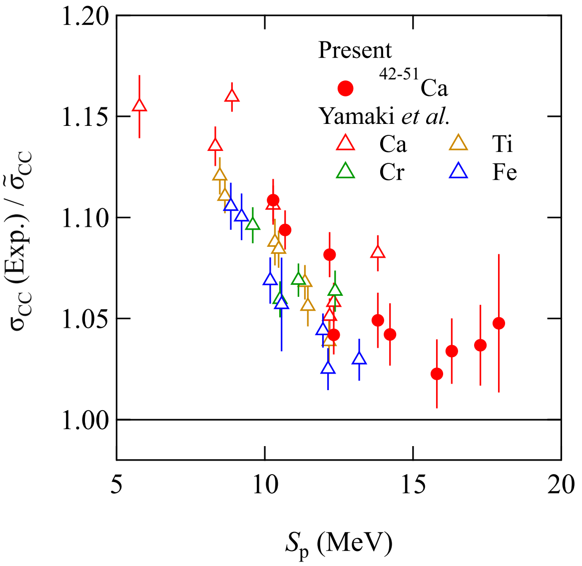

FIG. 6. Ratio of experimental σ_{CC} value to the $\tilde{\sigma}_{CC}$ value calculated using Eq. (12) as a function of one-proton separation energy S_p. The present results of $^{42-51}$Ca are indicated by the red closed circles. The open triangles represent the experimental results [20,21] of Ca (red), Ti (brown), Cr (green), and Fe (blue). The experimental σ_{CC} and calculated $\tilde{\sigma}_{CC}$ values of Ti, Cr, and Fe isotopes are illustrated in Figs. 9(d)–9(f) by the closed circles and the black solid lines, respectively.

calculation at lower S_p. The experimental σ_{CC} data decrease as S_p increases, and become closer to the Glauber-like calculation. This implies the importance of the proton binding strength in σ_{CC}.

B. Introduction of charged-particle evaporation induced by neutron-removal reaction

Strictly speaking, Eq. (12) is not based on microscopic theory because it is simply obtained from analogy with the Glauber-model calculation for σ_R. Using Eq. (9), the relationship between $\tilde{\sigma}_{CC}$ and σ_R defined by Eqs. (12) and (2) is [31]

$$\begin{aligned}\sigma_R &\equiv 2\pi\int b[1-T_p(b)T_n(b)]db\\ &= 2\pi\int b[1-T_p(b)]db\\ &\quad + 2\pi\int b[T_p(b)\{1-T_n(b)\}]db,\\ &\equiv \tilde{\sigma}_{CC}+\tilde{\sigma}_{\Sigma-xn},\end{aligned}\tag{16}$$

where $\tilde{\sigma}_{\Sigma-xn}$ is the total neutron-removal cross section without proton removal from the projectile nucleus. Bhagwat *et al.* previously noted the neutron-removal contribution to the charge-changing cross section, i.e., $\sigma_{CC} \neq \tilde{\sigma}_{CC}$ [31]. For this reason, Yamaguchi *et al.* introduced a correction factor [18].

To explicitly incorporate the neutron-removal reaction effect in the σ_{CC} calculation, the abrasion-ablation process [46], which consists of two processes to produce the reaction fragments, was considered in addition to the direct proton-removal process treated by the above Glauber-like model. The first stage is abrasion, where a prefragment with excitation energy is produced by abrading nucleons from the projectile nucleus. In the subsequent ablation stage, the prefragment is deexcited to the final fragment through light-particle or gamma-ray emission.

Here, the abrasion–ablation process was introduced similarly to Ref. [47]. Hence, σ_{CC} was defined as

$$\sigma_{CC} = \tilde{\sigma}_{CC} + \sigma_{evap},\tag{17}$$

where σ_{evap} is the neutron-removal cross section followed by the charged-particle evaporation and was calculated using the contribution probability of the neutron-removal reaction to σ_{CC}, P_{evap} (the online calculator for σ_{evap} is available [48]). Thus,

$$\sigma_{evap} = P_{evap}\tilde{\sigma}_{\Sigma-xn},\tag{18}$$

$$\begin{aligned}P_{evap} &= \sum_{x=1}^{N_P} p_{-xn}\\ &= \sum_{x=1}^{N_P} r_{-xn}\int_0^\infty w_{-xn}(E_{ex})f(E_{ex}, A_P-x, Z_P)dE_{ex}.\end{aligned}\tag{19}$$

Here, E_{ex} is the excitation energy of the prefragment; A_P, Z_P, and N_P are the projectile-nucleus mass number, atomic number, and neutron number, respectively; r_{-xn} is the ratio of the x-neutron removal cross section to that of total neutron removal; $w_{-xn}(E_{ex})$ is the excitation-energy distribution of the prefragment in each channel; and $f(E_{ex}, A_P-x, Z_P)$ is the probability of charged-particle evaporation for the prefragment with mass and atomic numbers A_P-x and Z_P, respectively, with E_{ex}. In addition, p_{-xn} is the partial value of P_{evap} regarding x.

1. Abrasion stage

The partial neutron-removal cross section $\tilde{\sigma}_{-xn}$ was expressed in the following binomial form, similar to the statistical abrasion model [46,49]:

$$\tilde{\sigma}_{-xn} = 2\pi\binom{N_P}{x}\int b\,T_p(b)[t_n(b)]^{N_P-x}[1-t_n(b)]^x db,\tag{20}$$

$$\begin{aligned}t_n(b) &= [T_n(b)]^{1/N_P}\\ &= \exp\left[-\int ds\left(\frac{\overline{\rho}_n^P}{N_P}\right)\left\{\sigma_{np}\overline{\rho}_p^T+\sigma_{nn}\overline{\rho}_n^T\right\}\right].\end{aligned}\tag{21}$$

Here, $t_n(b)$ represents the probability that a single neutron in the projectile transmits the target density. From Eq. (20), $\tilde{\sigma}_{\Sigma-xn}$ and r_{-xn} were calculated as

$$\tilde{\sigma}_{\Sigma-xn} = \sum_{x=0}^{N_P}\tilde{\sigma}_{-xn},\tag{22}$$

$$r_{-xn} = \frac{\tilde{\sigma}_{-xn}}{\tilde{\sigma}_{\Sigma-xn}}.\tag{23}$$

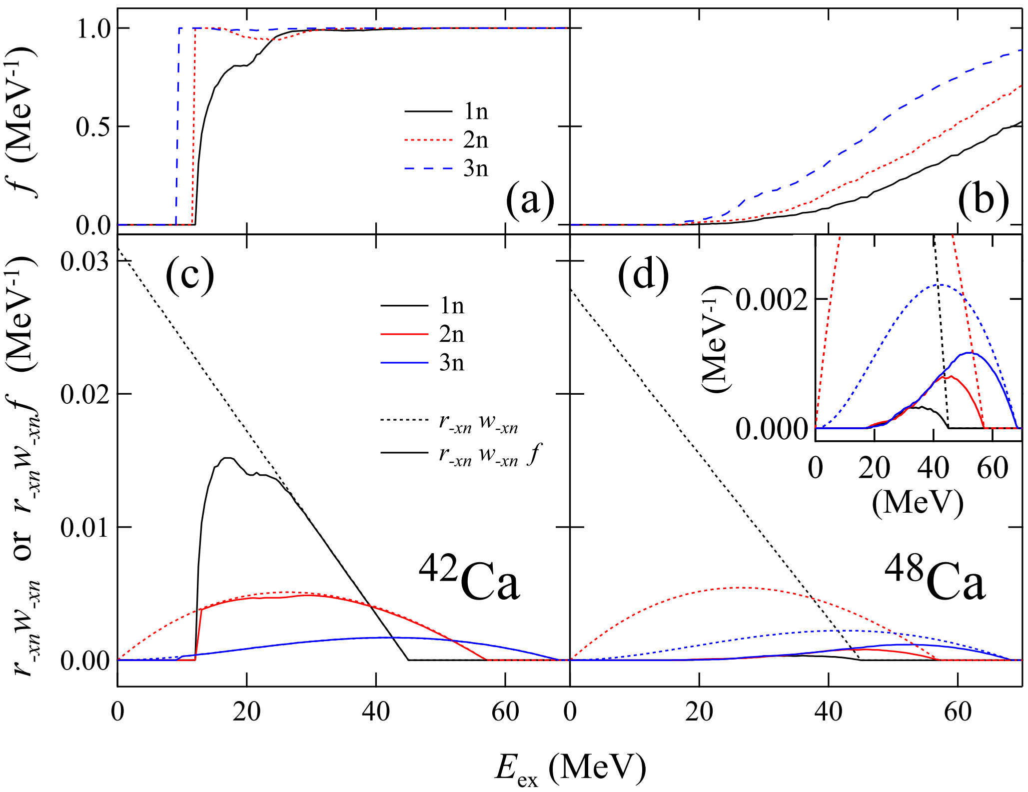

FIG. 7. (a,b) $f(E_{\rm ex}, A_{\rm P}-x, Z_{\rm P})$ of $1n$ (black), $2n$ (red), and $3n$ (blue) channels for ^{42}Ca and ^{48}Ca. (c,d) $E_{\rm ex}$ dependence of $r_{-xn}w_{-xn}(E_{\rm ex})$ (dotted) and $r_{-xn}w_{-xn}(E_{\rm ex})f(E_{\rm ex}, A_{\rm P}-x, Z_{\rm P})$ (solid) of the respective channels, where $E_{\rm max} = 45$ MeV. The inset of (d) shows a magnified view.

Note that the sum of $\tilde{\sigma}_{\rm CC}$ [Eq. (12)] and $\tilde{\sigma}_{\Sigma-xn}$ [Eq. (22)] is mathematically equal to $\sigma_{\rm R}$ [Eq. (2)]; i.e., Eq. (16) is strictly satisfied.

2. Prefragment excitation energy

The Gaimard-Schmidt method [46] was adopted to determine the prefragment excitation-energy distribution. In this method, the excitation energy distribution of the one-hole state via the single-nucleon removal, $g(\epsilon)$, is defined as

$$g(\epsilon) = \frac{2}{E_{\rm max}}\left(1 - \frac{\epsilon}{E_{\rm max}}\right). \tag{24}$$

This is a linear function satisfying the maximum excitation energy $E_{\rm max}$, i.e., $g(E_{\rm max}) = 0$ and $\int_0^{E_{\rm max}} g(\epsilon)d\epsilon = 1$. This functional shape corresponds to an approximation of the single-hole state density in the Woods-Saxon potential [50]. The excitation energy distribution $w_{-xn}(E_{\rm ex})$ via the abrasion of x neutrons is obtained from the convolution of $g(\epsilon)$:

$$w_{-xn}(E_{\rm ex}) = \frac{1}{x!}\int_0^\infty d\epsilon_1 \cdots d\epsilon_x \times \left[g(\epsilon_1)\cdots g(\epsilon_x) \times \delta\left(E_{\rm ex} - \sum_{i=1}^{x}\epsilon_i\right)\right]. \tag{25}$$

For the $\sigma_{\rm CC}$ calculation within this framework, the only free parameter is $E_{\rm max}$.

3. Ablation (evaporation) stage

The prefragment deexcitation process was treated using the statistical model, with $f(E_{\rm ex}, A_{\rm P}-x, Z_{\rm P})$ calculated using the GEMINI++ code [51–53]. This calculation reflects the light-particle or gamma-ray evaporation from the prefragment nucleus based on the Hauser-Feshbach theory. The yield distribution of the final fragment via the prefragment-nucleus decay was calculated using the Monte Carlo method for all sequential decays until no further decays occurred. Hence, we obtained $f(E_{\rm ex}, A_{\rm P}-x, Z_{\rm P})$ from the fraction of all decay channels with at least one charged-particle emission in the sequential decay. Here, the average angular momentum of the prefragment due to the peripheral fragmentation reaction was estimated to be at most $3\hbar$, even for a multineutron abraded channel (e.g., four neutrons) of ^{48}Ca [54]. For such a small angular momentum, $f(E_{\rm ex}, A_{\rm P}-x, Z_{\rm P})$ is largely independent on the initial angular momentum; therefore, the initial angular momentum was assumed to be zero here.

4. Contribution of respective xn channels to $P_{\rm evap}$

To illustrate the influence of each of the above components on $P_{\rm evap}$, calculations using $E_{\rm max} = 45$ MeV for ^{42,48}Ca are discussed as examples. In Figs. 7(c) and 7(d), results for $r_{-xn}w_{-xn}$ (the integral of which over $E_{\rm ex}$ and x is 1) are shown for channels up to three-neutron removal (dotted lines). The $r_{-xn}w_{-xn}$ distributions do not differ significantly between ^{42}Ca and ^{48}Ca. In contrast, a significant difference

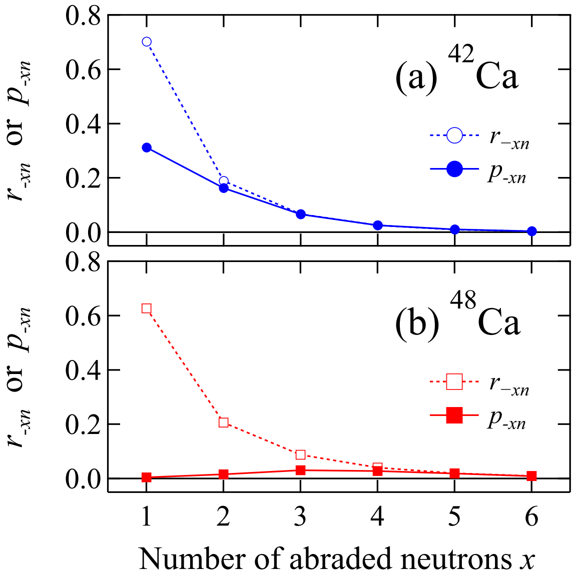

FIG. 8. r_{-xn} (open) and p_{-xn} (closed) of (a) ^{42}Ca (blue) and (b) ^{48}Ca (red) as functions of the number of removed neutrons x.

is apparent for $f(E_{\mathrm{ex}}, A_{\mathrm{P}} - x, Z_{\mathrm{P}})$ between these nuclides [Figs. 7(a) and 7(b)]. For ^{42}Ca, $f(E_{\mathrm{ex}}, A_{\mathrm{P}} - x, Z_{\mathrm{P}})$ of all channels immediately saturates to 1 beyond the threshold energy, which is the sum of the proton separation energy S_{p} and the Coulomb barrier energy E_{C}. However, the respective values of $f(E_{\mathrm{ex}}, A_{\mathrm{P}} - x, Z_{\mathrm{P}})$ for ^{48}Ca are far smaller than those for ^{42}Ca. Qualitatively, this can be interpreted as reflecting the fact that the ratio of the partial widths of the neutron and proton emissions in a single step $\Gamma_{\mathrm{n}}/\Gamma_{\mathrm{p}}$, which is dominant in the small E_{ex} region, roughly depends on [55]

$$\frac{\Gamma_{\mathrm{n}}}{\Gamma_{\mathrm{p}}} \simeq \frac{\exp\left[2\sqrt{a(E_{\mathrm{ex}} - S_{\mathrm{n}})}\right]}{\exp\left[2\sqrt{a(E_{\mathrm{ex}} - S_{\mathrm{p}} - E_{\mathrm{C}})}\right]}, \tag{26}$$

where a denotes the level density parameter. Thus, the competition between proton and neutron evaporation depends on the difference between S_{n} and S_{p}. This tendency generates a small $f(E_{\mathrm{ex}}, A_{\mathrm{P}} - x, Z_{\mathrm{P}})$ in the low-excitation-energy region for neutron-rich nuclides. Thus, for ^{48}Ca, $r_{-xn}w_{-xn}f$ [Fig. 7(d), solid lines] is distributed only in the high-excitation-energy region.

To clarify the above, r_{-xn} and p_{-xn}, which results from the integration of $r_{-xn}w_{-xn}f$ over E_{ex}, are plotted against the number of abraded neutrons in Fig. 8 (dotted and solid lines, respectively). For ^{42}Ca, 44% of the $1n$ channel (which accounts for approximately 70% of $\tilde{\sigma}_{\Sigma-xn}$) contributes to σ_{CC} with charged particle evaporation ($p_{-1n}/r_{-1n} = 0.31/0.70 = 0.44$). Most channels with more abraded neutrons contribute to σ_{CC}, yielding $P_{\mathrm{evap}} \equiv \sum p_{-xn} = 0.58$. In contrast, for ^{48}Ca, p_{-xn} is almost zero in channels below $3n$, yielding $P_{\mathrm{evap}} = 0.11$. Thus, P_{evap} strongly depends on the neutron number of the projectile nucleus. This dependence results in the decreasing trend of the experimental σ_{CC} data against N and S_{p} shown in Figs. 4 and 6.

C. Comparison of experimental and calculated results at $E \simeq 280$ MeV/nucleon

Hereafter, the calculation introducing the effects described in the previous subsection is denoted "Glauber(CE)." To perform this calculation, a 2pF-type function was assumed for the Ca-isotope $\rho_{\mathrm{n}}(r)$ used in Eq. (20). Similarly to $\rho_{\mathrm{p}}(r)$, $\rho_{\mathrm{n}}(0) = 0.088$ fm^{-3} was assumed. Under this constraint, for $^{42-51}$Ca, we employed a 2pF function that reproduced the experimental σ_{I} [7]. For $^{52-54}$Ca, σ_{I} values extrapolated from $^{48-51}$Ca were used. For ^{40}Ca, the parameters of the 2pF function were determined to reproduce the experimental r_{m} [56]. For $^{36-39}$Ca, the theoretical r_{m} values from the Hartree-Fock-Bogoliubov calculation with M3Y-P6a [57] were used to determine the parameters of the 2pF function.

In Fig. 4(b), the Glauber(CE) results for σ_{CC} on ^{12}C for Ca isotopes with $E_{\mathrm{max}} = 20$ and 70 MeV are represented by dashed and dotted thin black lines, respectively. These calculated results depend on the adopted value of E_{max}. From the chi-square fitting of the Glauber(CE) calculations to the present experimental σ_{CC} results for $^{42-51}$Ca, $E_{\mathrm{max}} = 45(8)$ MeV was obtained [Fig. 4(b), red line]. The corresponding P_{evap} [Fig. 4(a)] approaches zero asymptotically in the neutron-rich region, agreeing with the Glauber(ZROLA) calculation for $\tilde{\sigma}_{\mathrm{CC}}$ (black solid line).

The obtained $E_{\mathrm{max}} = 45(8)$ MeV can be understood by considering a naive Fermi gas model [46], where the typical Fermi energy is approximately 40 MeV. The E_{max} should be obtained when the single hole is located at the potential depth. Under this condition, the single-hole-state energy corresponds to the Fermi energy.

To examine this model for other isotopic chains, we compared the Glauber(CE) results with experimental values of σ_{CC} on ^{12}C at around 280 MeV/nucleon for Be [19], C [19,29,58,59], O [19,60], Ti [20], Cr [20], and Fe [20] isotopes. Here, $\rho_{\mathrm{p}}(r)$ and $\rho_{\mathrm{n}}(r)$ were assumed to be the 2pF functions for the Ti, Cr, and Fe isotopes. Harmonic-oscillator-type (HO) functions [61] were assumed for the Be, C, and O isotopes:

$$\rho(r) = \rho(0) \times \left[1 + \frac{C-2}{3}\left(\frac{r}{w}\right)^2\right] \exp\left[-\left(\frac{r}{w}\right)^2\right], \tag{27}$$

where C denotes the number of neutrons or protons, w is the radius parameter, and $\rho(0)$ is the normalization factor determined by the volume integral. For nuclides whose experimental r_{p} [1,44] and σ_{I} [16] results were available, the HO or 2pF function parameters reproducing these results were adopted, as for $^{42-51}$Ca. For ^{14}Be and the unstable C and O isotopes, no experimental r_{p} values have been determined other than from σ_{CC}; thus, the r_{p} values were taken from theoretical values via the fermionic molecular dynamics (FMD) [24], the coupled-cluster method with NNLO$_{\mathrm{sat}}$ [30], and relativistic mean field (RMF) calculations [30], which reproduce the experimental r_{p} values of stable nuclides in their respective isotopic chains [1]. In contrast, r_{p} for $^{55-58}$Cr were extrapolated from experimental r_{p} for $^{52-54}$Cr [1] in the same way as for ^{53,54}Ca mentioned before. The parameters for $\rho_{\mathrm{n}}(r)$ of the Ti, Cr, and Fe isotopes were selected to reproduce

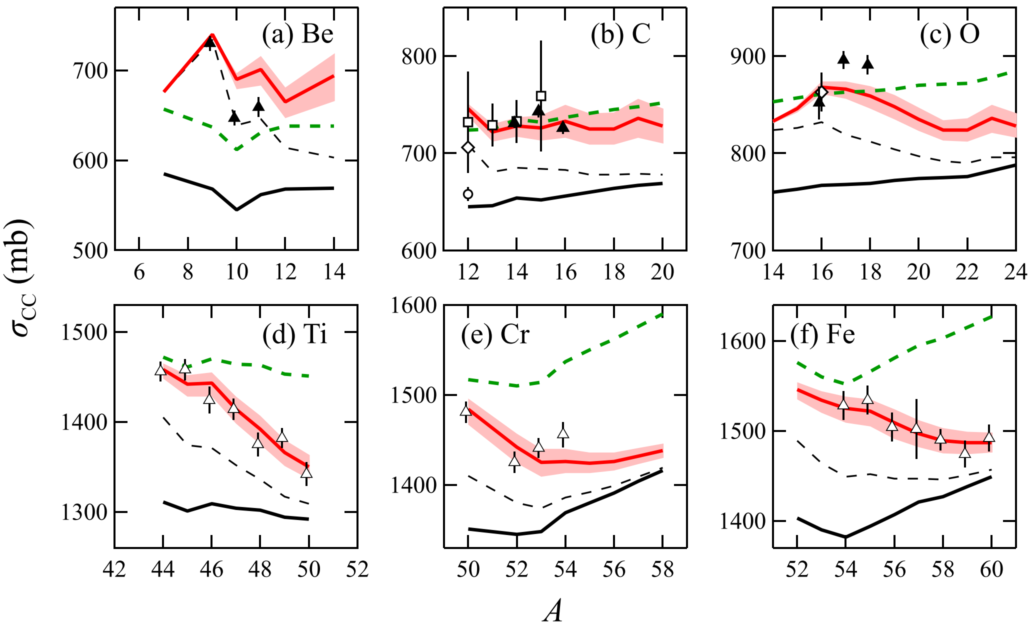

FIG. 9. Experimental $\sigma_{\rm CC}$ results at $E \simeq 280$ MeV/nucleon and Glauber(CE) $\sigma_{\rm CC}$ values for (a) Be, (b) C, (c) O, (d) Ti, (e) Cr, and (f) Fe isotopes as functions of A. The experimental results were taken from Refs. [19] (closed triangles), [20] (open triangles), [29] (open squares), [59,60] (open diamonds), and [58] (open circles). Each line is defined as in Fig. 4. The ratios of the experimental values to the calculated ones using Eq. (12) (black solid lines) for Ti, Cr, and Fe isotopes are represented in Fig. 6. The ratios of the experimental values to the Glauber(CR) calculations with $E_{\rm max} = 45$ MeV are represented in Fig. 10.

the theoretical $r_{\rm m}$ obtained via the Hartree-Fock–plus–BCS (HFBCS) calculations with the SkM* parameters [62–64].

The A dependences of $\sigma_{\rm CC}$ for respective isotopic chains at around 280 MeV/nucleon are shown in Fig. 9. In the figure, the experimental values decrease with increasing A for the Ca, Ti, Cr, and Fe isotopes, but are rather flat for the Be, C, and O isotopes. Notably, the Glauber(CE) calculations with $E_{\rm max} = 45$ MeV simultaneously reproduced the trends of the experimental results for various isotopic chains except for some data of Be isotopes and ^{12}C. Note that the existing results of ^{12}C [29,58,59] deviate from each other. The experimental results for Be isotopes are rather consistent with the Glauber(CE) calculation using $E_{\rm max} = 20$ MeV (thin black dashed line). Existing $\sigma_{\rm CC}$ calculation models (black-solid and green-dashed lines) cannot explain the experimental values for nuclides such as ^{9}Be, which are always accompanied by charged particle emissions via ^{8}Be according to the one-neutron removal. However, the Glauber(CE) successfully reproduced even the experimental value of ^{9}Be.

To quantitatively evaluate the Glauber(CE) method for nuclides with known $r_{\rm p}$, the ratios of the experimental $\sigma_{\rm CC}$ values to those of the Glauber(CE) calculations with $E_{\rm max} = 45$ MeV were plotted (Fig. 10). Here, in Fig. 10, only the experimental $\sigma_{\rm CC}$ data at around 280 MeV/nucleon were evaluated. The Glauber(CE) calculation reproduces the experimental data quite well. The standard deviation of the ratios, indicated by the shaded band in Fig. 10, around the mean ratio (1.004) is 1.6%, except for Be isotopes [Fig. 10(a)] and some ^{12}C data [open diamond and open circle in Fig. 10(b)]. In particular, the standard deviation was 0.9%, and the mean ratio was 1.001 for the present experimental data of Ca isotopes and existing data for Ti, Cr, and Fe isotopes. Thus, the Glauber(CE) calculation systematically explains the $\sigma_{\rm CC}$ data in several isotopic chains at around 280 MeV/nucleon by tuning just one parameter ($E_{\rm max}$) to reproduce Ca-isotope data, indicating the effect of charged-particle evaporation induced by neutron removal on $\sigma_{\rm CC}$ probably exists.

D. Derivation sensitivity of $\sigma_{\rm CC}$ to $r_{\rm p}$

Using the proposed calculation method, the relationship between $\sigma_{\rm CC}$ and the RMS radii of point-proton density distributions, $r_{\rm p}$, were investigated in Ca isotopes. In Fig. 11, the relationship between $r_{\rm p}$ and $\sigma_{\rm CC}$, calculated by the Glauber(CE) model with $E_{\rm max} = 45$ MeV, are illustrated by the red solid lines, considering the cases of ^{42}Ca and ^{51}Ca as examples. Here, as before, the central densities of $\rho_{\rm p}(r)$ and $\rho_{\rm n}(r)$ were assumed to be 0.088 fm^{-3}, and the other parameters of $\rho_{\rm n}(r)$ were determined to reproduce the existing experimental $\sigma_{\rm I}$ data [7]. Then, $\sigma_{\rm CC}$ was calculated by changing the parameters of $\rho_{\rm p}(r)$, i.e., by changing the $r_{\rm p}$ value.

As shown in Fig. 11, the correlation between $\sigma_{\rm CC}$ and $r_{\rm p}$ for ^{51}Ca has a steeper slope than that for ^{42}Ca. In other words, the sensitivity of $\sigma_{\rm CC}$ to $r_{\rm p}$ is small for nuclides near the beta-stability line, where the neutron removal reaction contributes to $\sigma_{\rm CC}$ through a large $P_{\rm evap}$ value, as shown in Fig. 4(a). In addition, to address the influence of the $E_{\rm max}$ uncertainty on the relation between $\sigma_{\rm CC}$ and $r_{\rm p}$, the calculation results using the Glauber(CE) with $E_{\rm max} = 45 \pm 8$ MeV are indicated by the red dashed lines in Fig. 11. In ^{42}Ca, the $E_{\rm max}$ uncertainty, that is the treatment of the evaporation process, also causes a non-negligible change in the relation between $\sigma_{\rm CC}$ and $r_{\rm p}$. Therefore, at the present, it might be difficult to deduce $r_{\rm p}$ from $\sigma_{\rm CC}$ with a good accuracy.

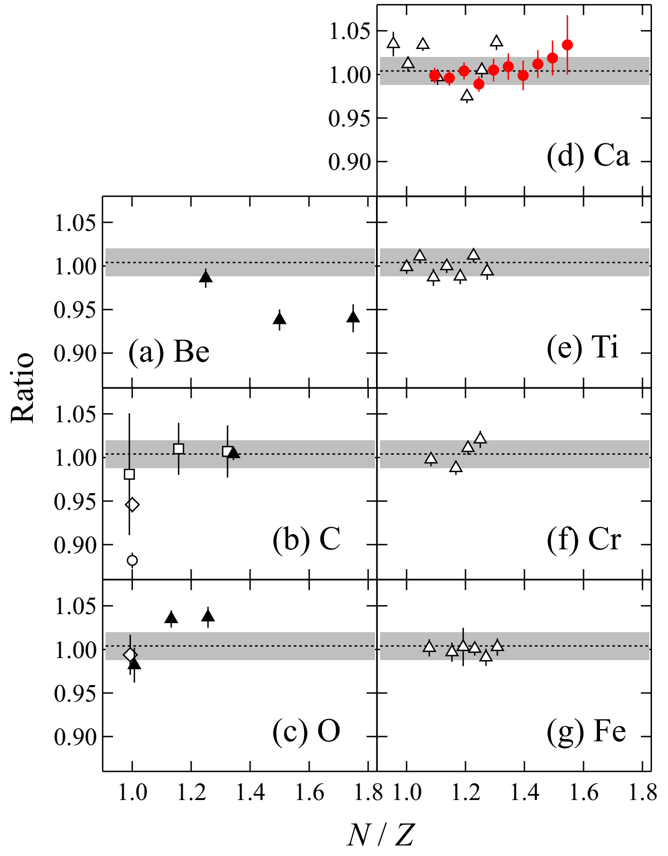

FIG. 10. Ratios of experimental σ_{CC} results on ^{12}C at around 280 MeV/nucleon to Glauber(CE) calculations for (a) Be, (b) C, (c) O, (d) Ca, (e) Ti, (f) Cr, and (g) Fe isotopes. Only the experimental data of nuclides, for which r_p were previously measured, are plotted. The marker symbols are the same as for Figs. 4 and 9. The shaded band shows the standard deviation (± 0.016) around ratio = 1.004 of the experimental data for nuclides from C to Fe isotopes, except for some ^{12}C data (open diamond and open circle).

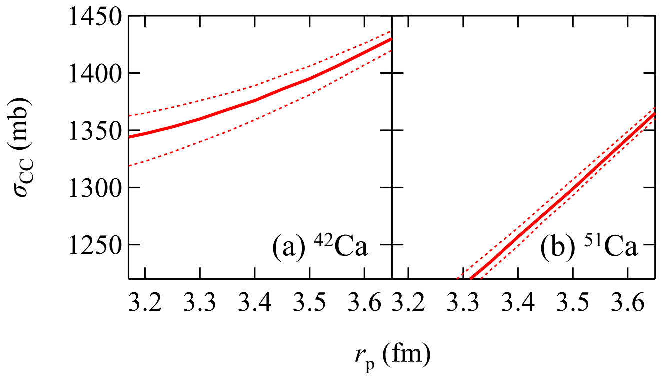

FIG. 11. Relation between r_p and σ_{CC} for (a) ^{42}Ca and (b) ^{51}Ca. The red solid lines indicate the calculations of σ_{CC} using the Glauber(CE) model with $E_{max} = 45$ MeV, while the red dashed lines indicate the uncertainty of the calculation owing to the E_{max} value (± 8 MeV).

On the other hand, the uncertainty of the relation between σ_{CC} and r_p for ^{51}Ca is significantly smaller than that for ^{42}Ca. For example, the change of r_p owing to the uncertainty of E_{max} with the same σ_{CC} value, i.e., the width between the dashed lines along the horizontal axis, is approximately ± 0.02 fm in ^{51}Ca, which is quite small, less than $\approx 1/5$ of that for ^{42}Ca. This is because the effect of charged-particle evaporation induced by the neutron removal on σ_{CC}, which corresponds to the difference between the red and black solid lines in Fig. 4, becomes negligible in the neutron-rich region. Hence, in such a region, the σ_{CC} data have the potential to extract r_p using a procedure similar to that used to deduce r_m from σ_R (for example, Refs. [6,7,16,65–74]).

To demonstrate the expected derivation accuracy of r_p, the relationship of the uncertainties of σ_{CC} and r_p is derived below in a simplified and general form. As shown in Eqs. (10) and (12), $\tilde{\sigma}_{CC}$ is a quantity that is sensitive to $\rho_p(r)$ of the projectile nucleus. From Eqs. (16), (17), and (18), the relationship between $\tilde{\sigma}_{CC}$ and σ_{CC}, which is an experimental observable, can be expressed as follows:

$$\tilde{\sigma}_{CC} = (1 - P_{evap})^{-1}\sigma_{CC} - \left(P_{evap}^{-1} - 1\right)^{-1}\sigma_R. \tag{28}$$

To simplify the discussion, the relationship between $\tilde{\sigma}_{CC}$ and r_p is expressed as

$$\tilde{\sigma}_{CC} \sim \pi(r_p + r_T)^2, \tag{29}$$

where r_T is the RMS matter radius of the target nucleus. From the above equations with the assumptions of $r_p \propto (2Z_P)^{1/3}$, where the RMS proton radius of the projectile nucleus was assumed to depend on the mass number of the self-conjugate isotope A_{SC}, i.e., $A_{SC} = 2Z_P$ (Z_P is the atomic number of projectile the nucleus), and $r_T \propto A_T^{1/3}$, the relation between the uncertainties of r_p and σ_{CC} is obtained as

$$\frac{\delta r_p}{r_p} \simeq \frac{1}{2}\left[1 + \left(\frac{A_T}{2Z_p}\right)^{1/3}\right] \times \left[\left\{1 + \left(P_{evap}^{-1} - 1\right)^{-1}\left(\frac{\sigma_R}{\tilde{\sigma}_{CC}}\right)\right\}^2 \left(\frac{\delta\sigma_{CC}}{\sigma_{CC}}\right)^2 + \left\{\left(P_{evap}^{-1} - 1\right)^{-1}\left(\frac{\sigma_R}{\tilde{\sigma}_{CC}}\right)\right\}^2 \left(\frac{\delta\sigma_R}{\sigma_R}\right)^2\right]^{1/2}. \tag{30}$$

Figure 12 shows the relative uncertainty of r_p, $\delta r_p/r_p$, for Ca isotopes, calculated using Eq. (30) as a function of A of Ca isotopes. In the calculations, the P_{evap} values using $E_{max} = 45$ MeV were adopted. It was also assumed that r_p is deduced from the σ_{CC} data on a carbon target with a condition of $\delta\sigma_{CC}/\sigma_{CC} = 1\%$. Here, the calculation results under the assumed relative uncertainties of 0%, 1%, and 3% in σ_R (or σ_I) are shown by the black dotted, red solid, and blue dashed lines, respectively. The uncertainty of σ_R does not affect the sensitivity of σ_{CC} to r_p in the neutron-rich region because all calculations converge to the same value. This results from the fact that the charged-particle evaporation induced by the neutron removal reaction is negligibly small in this region, as mentioned in Fig. 11. Fig.ure 12 also shows that r_p can be deduced with an accuracy of less than 1% from the σ_{CC} data

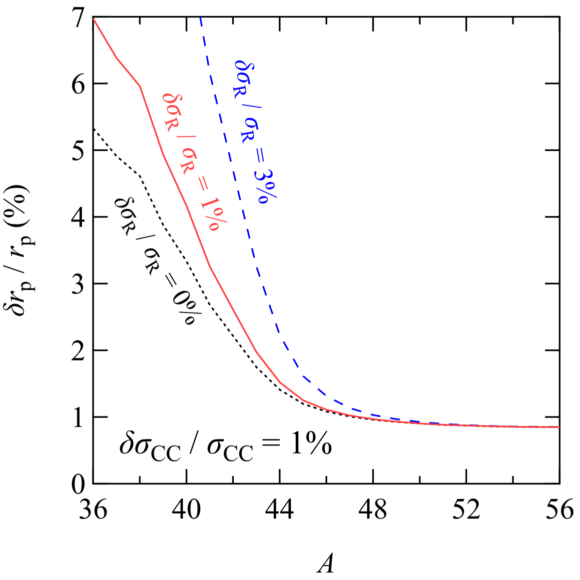

FIG. 12. Estimated relative uncertainty of the deduced r_p value from σ_{CC} of Ca isotopes as a function of A of projectile Ca isotopes. The P_{evap} values using $E_{max} = 45$ MeV were adopted. The $\delta\sigma_{CC}/\sigma_{CC}$ value was assumed to be 1%. The black dotted, red solid, and blue dashed lines indicate the results under the assumptions of $\delta\sigma_R/\sigma_R =$ 0%, 1%, and 3%, respectively. The estimation with the assumption of $\delta\sigma_R/\sigma_R = 3\%$ simulates the case wherein the experimental σ_R data are not available.

with $\delta\sigma_{CC}/\sigma_{CC} = 1\%$ for $A \geqslant 48$ when σ_R has already been measured with a typical accuracy of 1%. Note that σ_{cc} and σ_I (or σ_R) can be easily measured simultaneously as in the present study [7].

In contrast, in the nuclei for which the experimental σ_R or σ_I is unavailable, the theoretical σ_R value must be used instead of the experimental one. According to Refs. [75–77], the maximum deviation of the calculated σ_R value to the experimental one [7] is at most 3% in $^{42–51}$Ca. To simulate this, the $\delta r_p/r_p$ values assuming $\delta\sigma_R/\sigma_R = 3\%$ were indicated by the blue dashed line in Fig. 12. This result demonstrates that r_p can be deduced with 0.9% accuracy from the σ_{CC} data with $\delta\sigma_{CC}/\sigma_{CC} = 1\%$ for Ca isotopes for $A \geqslant 51$ even if the experimental σ_R value is unavailable. Note that even if we assume the 6% uncertainty for σ_R (twice the value used for the blue dashed line), the r_p values for Ca isotopes for $A \geqslant 52$ can be still deduced with 0.9% accuracy from the σ_{CC} data. Thus, the σ_{CC} measurement at $E \simeq 280$ MeV/nucleon can be utilized to deduce the r_p of a neutron-rich nucleus.

E. Comparison of experimental and calculated results in other energy regions

There are systematic σ_{CC} data to derive r_p at energies other than $E \simeq 280$ MeV/nucleon [17,18,24–27]. Therefore, it would be valuable to evaluate the Glauber(CE) calculation in other energy regions.

First, the experimental σ_{CC} values on ^{12}C at around 900 MeV/nucleon [17,24–27,58] were compared. As for the C isotopes above, the $\rho_p(r)$ and $\rho_n(r)$ of the B, N, and F isotopes were assumed to be the HO functions that reproduce the theoretical r_p and experimental σ_I [16,78]. As r_p values to be reproduced, the anti-symmetrized molecular dynamics (AMD) [79] theoretical values scaled to fit the experimental r_p of ^{11}B [1] were used for the B isotopes, the theoretical values from the in-medium similarity renormalization group (VS-IMSRG) [27], which reproduce the experimental r_p of ^{14}N [1], were used for the N isotopes, and the theoretical values from the HFBCS with the SkM* [62–64], which also reproduce the experimental r_p of ^{19}F [1], were used for the F isotopes.

The experimental and calculated values are presented in Fig. 13. Note that although the calculation using the correction factor (green dashed line) has been validated between 100 and 600 MeV/nucleon in Ref. [18], the comparison with this method also at 900 MeV/nucleon would be valuable. Experimental σ_{CC} results without the correction of the neutron-removal cross section were taken from Refs. [25–27], except for those for ^{7,9}Be [24]. In Ref. [27], two types of experimental values that depend on the analysis method were reported for N isotopes. Both values, labeled by $\sigma_{cc}^{ex,\mathrm{veto}}$ and $\sigma_{cc}^{ex,\mathrm{noveto}}$ in Ref. [27], are plotted as solid and open triangles in Fig. 13(d), respectively. The existing experimental data deviate from each other systematically depending on the datasets in some isotopic chains. The Glauber(CE) calculations with $E_{max} = 45$ MeV overestimated several values of the Be, B, C, and N isotopes, as shown by the closed triangles [24–27], open circle [24], and open diamond [58], and also overestimated the values of O isotopes (crosses). The Glauber(ZROLA) calculations with the correction factor (green dashed line) and/or the Glauber(CE) calculations with $E_{max} = 20$ MeV (thin black dashed line) were rather consistent with these experimental data. In contrast, the experimental values shown by crosses [17] (except for O isotopes) and open triangles ($\sigma_{cc}^{ex,\mathrm{noveto}}$ [27]) agreed relatively well with the Glauber(CE) calculations under the same E_{max} as for the data at 280 MeV/nucleon (red line).

Then, the energy dependence of the experimental σ_{CC} on ^{12}C for ^{28}Si [18,58,80,81] was compared to the Glauber(CE) results (Fig. 14), for the same ^{28}Si density profiles as in Ref. [18]. The Glauber(CE) results with $E_{max} =$ 45(8) MeV overestimated the experimental results in $E < 200$ MeV/nucleon. On the other hand, at higher energies, the calculation agreed well with some experimental values. However, as in Fig. 13, the experimental data in Fig. 14 also show deviations beyond respective uncertainties from each other, especially at $E > 700$ MeV. Therefore, to understand the σ_{CC} data at energies other than around 280 MeV/nucleon in more detail, future studies based on more sophisticated theories are strongly desired.

IV. SUMMARY

In summary, we performed σ_{CC} measurements for $^{42–51}$Ca on a carbon target at around 280 MeV/nucleon. The obtained σ_{CC} results decreased significantly with increasing A, differing from the trend for light-mass isotopic chains such as C isotopes. The overall experimental trend could not be explained by Glauber-like calculations. To explain the results

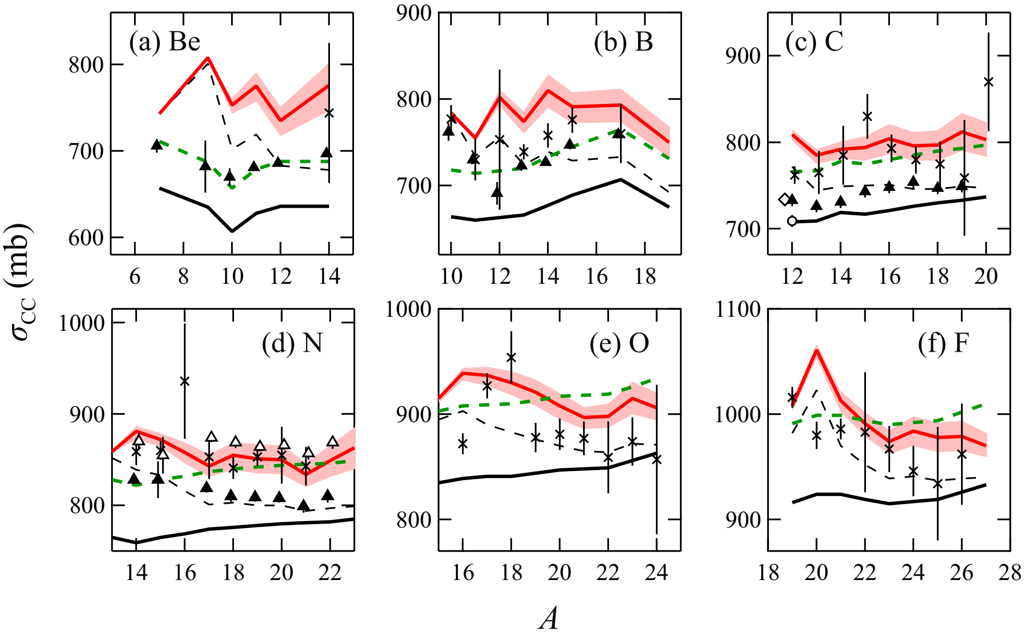

FIG. 13. Experimental σ_{CC} results at $E \simeq 900$ MeV/nucleon and Glauber(CE) values of σ_{CC} for (a) Be, (b) B, (c) C, (d) N, (e) O, and (f) F isotopes as functions of A. The systematic experimental results are represented by crosses [17] and closed triangles [24–27]. The open triangles in (d) indicate $\sigma_{CC}^{ex,\mathrm{noveto}}$ values from Ref. [27]. The open diamond and circle indicate experimental values from Refs. [24] and [58], respectively. Each line is defined as in Fig. 4.

of Ca isotopes, the charged-particle evaporation effect induced by the neutron-removal reaction was introduced. From the experimental σ_{CC} data for $^{42-51}$Ca, the parameter of the Glauber(CE) model, $E_{\max}$, was determined to be 45(8) MeV, and experimental σ_{CC} values at around 280 MeV/nucleon were successfully explained for other isotopic chains from C to Fe by the current model. The standard deviation between these experimental results and the calculations was 1.6% for the C to Fe isotopes and, notably, 0.9% for isotopes beyond Ca. The comparison between experimental and calculated results also clarifies that the charged-particle evaporation effect is negligibly small in the neutron-rich region, indicating the σ_{CC} data potentially allow one to extract r_p of very neutron-rich unstable nuclei; these values are difficult to measure using other experimental methods. The sensitivity of σ_{CC} to r_p was also evaluated. As a result, it was demonstrated that a σ_{CC} with an accuracy of 1% is sensitive enough to determine the r_p with an accuracy of 0.9% for neutron-rich Ca isotopes ($A \geqslant 50$). The Glauber(CE) model was also evaluated in other energy regions, and some σ_{CC} data were reproduced using the proposed calculation model. To understand σ_{CC} in more detail, especially in energy regions other than around 280 MeV/nucleon, future studies based on more sophisticated theories are required.

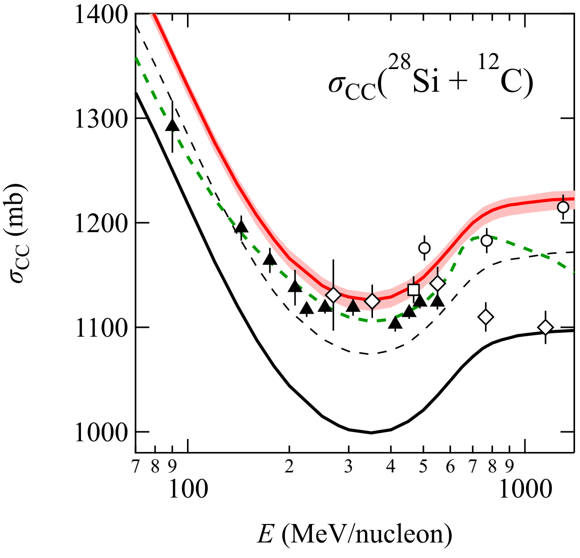

FIG. 14. Energy dependence of σ_{CC} for ^{28}Si on ^{12}C. The experimental values are represented by closed triangles [18], open circles [58], open diamonds [80], and open squares [81]. Each line is defined as in Fig. 4.

ACKNOWLEDGMENTS

We would like to express our gratitude to the accelerator staff at RIKEN Nishina Center for providing the intense ^{238}U beam. We are grateful to R. J. Charity for providing the latest version of the GEMINI++ code. Discussions of the statistical decay codes with S. Ebata, C. Ishizuka, and K. Sekizawa are also gratefully acknowledged. The present work was supported by JSPS KAKENHI Grants No. JP24244024, No. JP15J01446, No. JP16H03905, and No. JP21K13947.

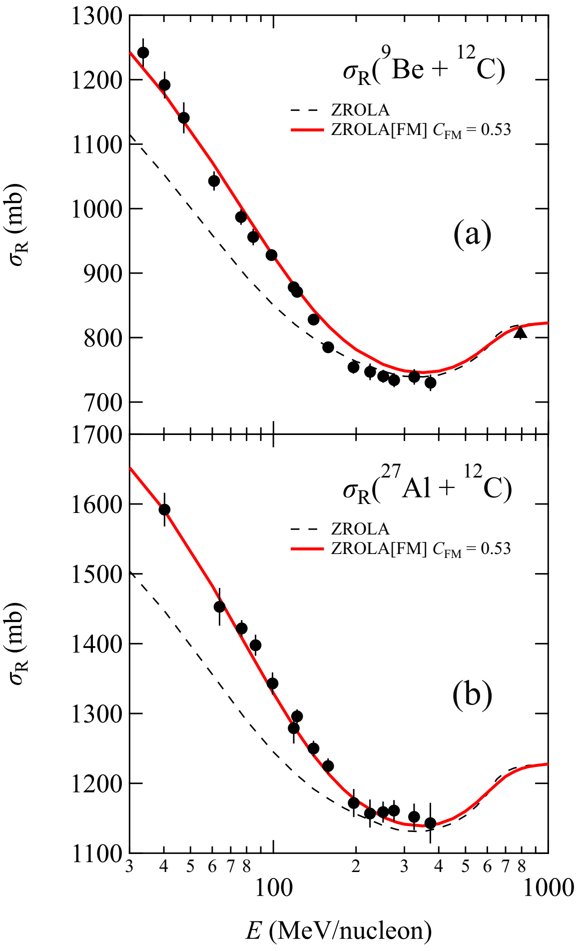

FIG. 15. Energy dependence of σ_R for (a) ^{9}Be and (b) ^{27}Al on ^{12}C [16,38,39]. The red solid and black dotted lines indicate the present ZROLA calculation with the best-fit parameter for the Fermi motion, $C_{FM} = 0.53$, and the conventional ZROLA calculation without the Fermi motion effect on σ_{ij}, respectively. The experimental data are taken from Ref. [16] (triangle) and Ref. [38] (circles).

APPENDIX A: COMPARISON OF REACTION CROSS SECTION DATA TO GLAUBER-MODEL CALCULATION APPLIED IN THIS WORK

To demonstrate the validity of the Glauber-model calculation used in this work, we compare the Glauber-model calculations to the σ_R data for ^{9}Be and ^{27}Al on ^{12}C. The experimental values were taken from Ref. [16,38]. In the calculation, the point-proton and point-neutron density distributions introduced in Ref. [38] were used as the density profiles of ^{9}Be and ^{27}Al.

Figure 15 shows the energy dependences of σ_R for ^{9}Be and ^{27}Al on ^{12}C. Thus, the Glauber-model calculation applied in this work not only systematically reproduces the σ_R data of $^{12}\text{C} + ^{12}\text{C}$ shown in Fig. 5, but also the data of other reaction systems.

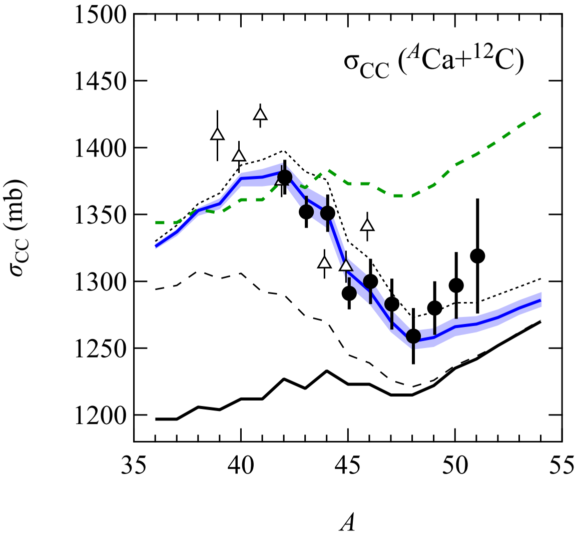

FIG. 16. Same as Fig. 4(b), but with the Glauber-model calculations without the Fermi-motion effect under the ZROLA. The blue solid line and the corresponding shaded region indicate the Glauber(CE) model with $E_{max} = 55(6)$ MeV. The black solid line and green dashed line represent the σ_{CC} values from the Glauber(ZROLA) calculation [Eq. (12)] and the Glauber(ZROLA) calculation with the correction factor [18] [Eq. (13)], respectively. The present $^{42-51}$Ca results and existing data [20,21] are indicated by closed circles and open triangles, respectively.

APPENDIX B: DISCUSSION BASED ON GLAUBER-MODEL CALCULATION WITHOUT EFFECT OF FERMI MOTION

In this study, we used the Glauber-model calculation taking the Fermi-motion effect into account. From the comparison between the two calculations shown in Figs. 5 and 15, the reproducibility of the σ_R data below 200 MeV/nucleon was improved by the calculation with the Fermi-motion effect. This agreement in σ_R in a wide energy region is important to evaluate the energy dependence of σ_{CC} shown in Fig. 14.

On the other hand, these two types of the Glauber-model calculations give almost the same σ_R values in $E \geqslant 200$ MeV/nucleon. In Fig. 5, for example, the differences between these calculations in σ_R for ^{12}C on ^{12}C at 280 MeV/nucleon and 900 MeV/nucleon are 1.3% and 0.05%, respectively. Therefore, the adopted model for the Glauber-model calculation does not influence the essence of the discussion in this paper.

In Fig. 16, the calculation results of σ_{CC} for Ca isotopes on ^{12}C by the Glauber-model calculations without the Fermi-motion effect under the ZROLA are shown. In this calculation, the bare NN cross sections $\sigma_{NN}^{\text{bare}}$ were used instead of the effective ones σ_{NN}^{eff} defined in Eq. (4). Compared to Fig. 4(b), the $\tilde{\sigma}_{CC}$ values (black solid line) in Fig. 16 are 1.3% smaller. As a result, the obtained value of E_{max}, which contributes to the other term in σ_{CC}, i.e., σ_{evap} [see Eq. (18)], was 55(6) MeV. This value is slightly larger than the one mentioned in the main discussion of the paper [$E_{max} = 45(8)$ MeV]. However, the Glauber(CE) calculation with $E_{max} = 55(6)$ MeV (blue

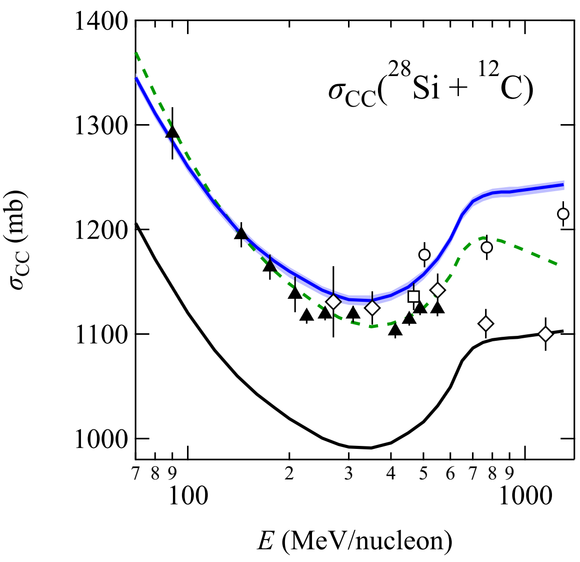

FIG. 17. Same as Fig. 14, but with the Glauber-model calculations without the Fermi-motion effect under the ZROLA. The definitions of all the lines are the same as in Fig. 16. The experimental values are represented by closed triangles [18], open circles [58], open diamonds [80], and open squares [81].

line in Fig. 16) still accurately reproduces the trend of experimental σ_{CC} data at around 280 MeV/nucleon, not only for Ca isotopes but also for other isotopes shown in Fig. 9, similarly to the Glauber(CE) calculation with the Fermi-motion effect using $E_{max} = 45(8)$ MeV. Therefore, the importance of the effect of charged-particle evaporation induced by the neutron removal reaction on σ_{CC} does not change.

In Fig. 17, the blue line shows the calculated energy dependence of σ_{CC} for ^{28}Si on ^{12}C by the Glauber(CE) model without the Fermi-motion effect using $E_{max} = 55(6)$ MeV. Below 200 MeV/nucleon, the Glauber(CE) calculation without the Fermi motion are rather consistent with the experimental data. However, this calculation fails to reproduce σ_R data in this energy region, as shown in Fig. 5 and Appendix A.

At high energies around 900 MeV/nucleon, the $\tilde{\sigma}_{CC}$ value is independent of the Fermi motion effect for the Glauber-like model similar to σ_R mentioned above. Therefore, with an increase in the value of E_{max} from 45 MeV to 55 MeV, the calculated value of σ_{CC} using the Glauber(CE) model without the Fermi motion effect also increases. Figure 17 shows σ_{CC} for ^{28}Si on ^{12}C as a function of energy. Compared to Fig. 14, the calculated σ_{CC} value at around 900 MeV/nucleon by the Glauber(CE) model (blue solid line) in Fig. 17 increases by about 1.6%. Although the Glauber(CE) calculation with the Fermi motion effect using $E_{max} = 45(8)$ MeV agrees with some of the existing data at $E > 700$ MeV/nucleon, as shown by the red line in Fig. 14, the calculation without the Fermi motion using $E_{max} = 55(6)$ MeV shown by the blue line in Fig. 17 overestimates all the existing data.

Therefore, to maintain the consistency of the agreement between the experimental data and the calculations both in σ_R at $E = 30$–1000 MeV/nucleon and σ_{CC} at $E > 200$ MeV/nucleon, we applied the Glauber model with the Fermi motion effect. In future work, it will be interesting to investigate the energy dependence of σ_{CC} in detail.

[1] I. Angeli and K. P. Marinova, At. Data Nucl. Data Tables **99**, 69 (2013).

[2] L. B. Wang, P. Mueller, K. Bailey, G. W. F. Drake, J. P. Greene, D. Henderson, R. J. Holt, R. V. F. Janssens, C. L. Jiang, Z. T. Lu, T. P. O'Connor, R. C. Pardo, K. E. Rehm, J. P. Schiffer, and X. D. Tang, Phys. Rev. Lett. **93**, 142501 (2004).

[3] R. Sánchez, W. Nörtershäuser, G. Ewald, D. Albers, J. Behr, P. Bricault, B. A. Bushaw, A. Dax, J. Dilling, M. Dombsky, G. W. F. Drake, S. Götte, R. Kirchner, H.-J. Kluge, T. Kühl, J. Lassen, C. D. P. Levy, M. Pearson, E. Prime, V. Ryjkov, A. Wojtaszek, Z. C. Yan, and C. Zimmermann, Phys. Rev. Lett. **96**, 033002 (2006).

[4] R. F. Garcia Ruiz *et al.*, Nat. Phys. **12**, 594 (2016).

[5] C. Gorges, L. V. Rodriguez, D. L. Balabanski, M. L. Bissell, K. Blaum, B. Cheal, R. F. GarciaRuiz, G. Georgiev, W. Gins, H. Heylen, A. Kanellakopoulos, S. Kaufmann, M. Kowalska, V. Lagaki, S. Lechner, B. Maass, S. Malbrunot-Ettenauer, W. Nazarewicz, R. Neugart, G. Neyens *et al.*, Phys. Rev. Lett. **122**, 192502 (2019).

[6] T. Suzuki, H. Geissel, O. Bochkarev, L. Chulkov, M. Golovkov, D. Hirata, H. Irnich, Z. Janas, H. Keller, T. Kobayashi, G. Kraus, G. Münzenberg, S. Neumaier, F. Nickel, A. Ozawa, A. Piechaczeck, E. Roeckl, W. Schwab, K. Sümmerer, K. Yoshida, and I. Tanihata, Phys. Rev. Lett. **75**, 3241 (1995).

[7] M. Tanaka *et al.*, Phys. Rev. Lett. **124**, 102501 (2020).

[8] B. A. Brown, Phys. Rev. Lett. **85**, 5296 (2000).

[9] D. Nishimura *et al.*, Nucl. Phys. A **834**, 470c (2010).

[10] T. Moriguchi, A. Ozawa, S. Ishimoto, Y. Abe, M. Fukuda, I. Hachiuma, Y. Ishibashi, Y. Ito, T. Kuboki, M. Lantz, D. Nagae, K. Namihira, D. Nishimura, T. Ohtsubo, H. Ooishi, T. Suda, H. Suzuki, T. Suzuki, M. Takechi, K. Tanaka, and T. Yamaguchi, Phys. Rev. C **88**, 024610 (2013).

[11] W. Horiuchi, Y. Suzuki, and T. Inakura, Phys. Rev. C **89**, 011601(R) (2014).

[12] H. Sakaguchi and J. Zenihiro, Prog. Part. Nucl. Phys. **97**, 1 (2017).

[13] T. Suda, M. Wakasugi, T. Emoto, K. Ishii, S. Ito, K. Kurita, A. Kuwajima, A. Noda, T. Shirai, T. Tamae, H. Tongu, S. Wang, and Y. Yano, Phys. Rev. Lett. **102**, 102501 (2009).

[14] M. Wakasugi *et al.*, Nucl. Instrum. Methods Phys. Res., Sect. B **317**, 668 (2013).

[15] K. Tsukada, A. Enokizono, T. Ohnishi, K. Adachi, T. Fujita, M. Hara, M. Hori, T. Hori, S. Ichikawa, K. Kurita, K. Matsuda, T. Suda, T. Tamae, M. Togasaki, M. Wakasugi, M. Watanabe, and K. Yamada, Phys. Rev. Lett. **118**, 262501 (2017).

[16] A. Ozawa, T. Suzuki, and I. Tanihata, Nucl. Phys. A **693**, 32 (2001).

[17] L. V. Chulkov *et al.*, Nucl. Phys. A **674**, 330 (2000).

[18] T. Yamaguchi, M. Fukuda, S. Fukuda, G. W. Fan, I. Hachiuma, M. Kanazawa, A. Kitagawa, T. Kuboki, M. Lantz, M. Mihara,

M. Nagashima, K. Namihira, D. Nishimura, Y. Okuma, T. Ohtsubo, S. Sato, T. Suzuki, M. Takechi, and W. Xu, Phys. Rev. C **82**, 014609 (2010).

[19] T. Yamaguchi, I. Hachiuma, A. Kitagawa, K. Namihira, S. Sato, T. Suzuki, I. Tanihata, and M. Fukuda, Phys. Rev. Lett. **107**, 032502 (2011).

[20] S. Yamaki *et al.*, Nucl. Instrum. Methods Phys. Res. B **317**, 774 (2013).

[21] S. Yamaki *et al.*, EPJ Web Conf. **66**, 03099 (2014).

[22] A. Ozawa, T. Moriguchi, T. Ohtsubo, N. Aoi, D. Q. Fang, N. Fukuda, M. Fukuda, H. Geissel, I. Hachiuma, N. Inabe, Y. Ishibashi, S. Ishimoto, Y. Ito, T. Izumikawa, D. Kameda, T. Kubo, T. Kuboki, K. Kusaka, M. Lantz *et al.*, Phys. Rev. C **89**, 044602 (2014).

[23] K. Sawahata *et al.*, Nucl. Phys. A **961**, 142 (2017).

[24] S. Terashima *et al.*, Prog. Theor. Exp. Phys. **2014**, 101D02 (2014).

[25] A. Estrade, R. Kanungo, W. Horiuchi, F. Ameil, J. Atkinson, Y. Ayyad, D. Cortina-Gil, I. Dillmann, A. Evdokimov, F. Farinon, H. Geissel, G. Guastalla, R. Janik, M. Kimura, R. Knobel, J. Kurcewicz, Y. A. Litvinov, M. Marta, M. Mostazo, I. Mukha *et al.*, Phys. Rev. Lett. **113**, 132501 (2014).

[26] R. Kanungo, W. Horiuchi, G. Hagen, G. R. Jansen, P. Navratil, F. Ameil, J. Atkinson, Y. Ayyad, D. Cortina-Gil, I. Dillmann, A. Estrade, A. Evdokimov, F. Farinon, H. Geissel, G. Guastalla, R. Janik, M. Kimura, R. Knobel, J. Kurcewicz *et al.*, Phys. Rev. Lett. **117**, 102501 (2016).

[27] S. Bagchi *et al.*, Phys. Lett. B **790**, 251 (2019).

[28] D. T. Tran, H. J. Ong, T. T. Nguyen, I. Tanihata, N. Aoi, Y. Ayyad, P. Y. Chan, M. Fukuda, T. Hashimoto, T. H. Hoang, E. Ideguchi, A. Inoue, T. Kawabata, L. H. Khiem, W. P. Lin, K. Matsuta, M. Mihara, S. Momota, D. Nagae, N. D. Nguyen *et al.*, Phys. Rev. C **94**, 064604 (2016).

[29] J. Zhao *et al.*, JPS Conf. Proc. **32**, 010023 (2020).

[30] D. T. Tran *et al.*, Nat. Commun. **9**, 1594 (2018).

[31] A. Bhagwat and Y. K. Gambhir, Phys. Rev. C **69**, 014315 (2004).

[32] T. Akaishi and K. Hagino, JPS Conf. Proc. **6**, 030097 (2015).

[33] Y. Suzuki, W. Horiuchi, S. Terashima, R. Kanungo, F. Ameil, J. Atkinson, Y. Ayyad, D. Cortina-Gil, I. Dillmann, A. Estrade, A. Evdokimov, F. Farinon, H. Geissel, G. Guastalla, R. Janik, R. Knoebel, J. Kurcewicz, Y. A. Litvinov, M. Marta, M. Mostazo, I. Mukha *et al.*, Phys. Rev. C **94**, 011602(R) (2016).

[34] T. Kubo *et al.*, Prog. Theor. Exp. Phys. **2012**, 03C003 (2012).

[35] I. Tanihata, H. Savajols, and R. Kanungo, Prog. Part. Nucl. Phys. **68**, 215 (2013).

[36] B. Abu-Ibrahim and Y. Suzuki, Phys. Rev. C **61**, 051601(R) (2000).

[37] W. Horiuchi, Y. Suzuki, B. Abu-Ibrahim, and A. Kohama, Phys. Rev. C **75**, 044607 (2007).

[38] M. Takechi, M. Fukuda, M. Mihara, K. Tanaka, T. Chinda, T. Matsumasa, M. Nishimoto, R. Matsumiya, Y. Nakashima, H. Matsubara, K. Matsuta, T. Minamisono, T. Ohtsubo, T. Izumikawa, S. Momota, T. Suzuki, T. Yamaguchi, R. Koyama, W. Shinozaki, M. Takahashi *et al.*, Phys. Rev. C **79**, 061601(R) (2009).

[39] A. Ozawa *et al.*, Nucl. Phys. A **691**, 599 (2001).

[40] A. S. Goldhaber, Phys. Lett. B **53**, 306 (1974).

[41] H. Atac, M. Constantinou, Z.-E. Meziani, M. Paolone, and N. Sparveris, Nat. Commun. **12**, 1759 (2021).

[42] C. Patrignani, Chin. Phys. C **40**, 100001 (2016).

[43] A. J. Miller *et al.*, Nat. Phys. **15**, 432 (2019).

[44] K. Minamisono, D. M. Rossi, R. Beerwerth, S. Fritzsche, D. Garand, A. Klose, Y. Liu, B. Maaß, P. F. Mantica, A. J. Miller, P. Müller, W. Nazarewicz, W. Nörtershäuser, E. Olsen, M. R. Pearson, P. G. Reinhard, E. E. Saperstein, C. Sumithrarachchi, and S. V. Tolokonnikov, Phys. Rev. Lett. **117**, 252501 (2016).

[45] M. Wang, W. J. Huang, F. G. Kondev, G. Audi, and S. Naimi, Chin. Phys. C **45**, 030003 (2021).

[46] J.-J. Gaimard and K.-H. Schmidt, Nucl. Phys. A **531**, 709 (1991).

[47] C. Scheidenberger, I. A. Pshenichnov, K. Sümmerer, A. Ventura, J. P. Bondorf, A. S. Botvina, I. N. Mishustin, D. Boutin, S. Datz, H. Geissel, P. Grafström, H. Knudsen, H. F. Krause, B. Lommel, S. P. Møller, G. Münzenberg, R. H. Schuch, E. Uggerhøj, U. Uggerhoj, C. R. Vane, Z. Z. Vilakazi, and H. Weick, Phys. Rev. C **70**, 014902 (2004).

[48] https://www.isotopea.com/nurex/.

[49] C. A. Bertulani and P. Danielewicz, *Introduction to Nuclear Reactions* (CRC, London, 2004).

[50] K.-H. Schmidt, H. Delagrange, J. P. Dufour, N. Carjan, and A. Fleury, Z. Phys. A **308**, 215 (1982).

[51] R. J. Charity, Phys. Rev. C **82**, 014610 (2010).

[52] D. Mancusi, R. J. Charity, and J. Cugnon, Phys. Rev. C **82**, 044610 (2010).

[53] http://lise.nscl.msu.edu/porting/gemini.html.

[54] M. de Jong, A. V. Ignatyuk, and K. H. Schmidt, Nucl. Phys. A **613**, 435 (1997).

[55] J. Benlliure *et al.*, Eur. Phys. J. A **2**, 193 (1998).

[56] J. Zenihiro *et al.*, arXiv:1810.11796.

[57] H. Nakada, Phys. Rev. C **100**, 044310 (2019).

[58] W. R. Webber, J. C. Kish, and D. A. Schrier, Phys. Rev. C **41**, 520 (1990).

[59] C. Zeitlin, S. Guetersloh, L. Heilbronn, J. Miller, A. Fukumura, Y. Iwata, and T. Murakami, Phys. Rev. C **76**, 014911 (2007).

[60] C. Zeitlin, J. Miller, S. Guetersloh, L. Heilbronn, A. Fukumura, Y. Iwata, T. Murakami, S. Blattnig, R. Norman, and S. Mashnik, Phys. Rev. C **83**, 034909 (2011).

[61] K. Tanaka, M. Fukuda, M. Mihara, M. Takechi, D. Nishimura, T. Chinda, T. Sumikama, S. Kudo, K. Matsuta, T. Minamisono, T. Suzuki, T. Ohtsubo, T. Izumikawa, S. Momota, T. Yamaguchi, T. Onishi, A. Ozawa, I. Tanihata, and T. Zheng, Phys. Rev. C **82**, 044309 (2010).

[62] InPACS/CCS, University of Tsukuba, http://wwwnucl.ph.tsukuba.ac.jp/InPACS/.

[63] S. Ebata and T. Nakatsukasa, Phys. Scr. **92**, 064005 (2017).

[64] S. Ebata, T. Nakatsukasa, and T. Inakura, Phys. Rev. C **90**, 024303 (2014).

[65] I. Tanihata *et al.*, Phys. Lett. B **160**, 380 (1985).

[66] I. Tanihata, H. Hamagaki, O. Hashimoto, Y. Shida, N. Yoshikawa, K. Sugimoto, O. Yamakawa, T. Kobayashi, and N. Takahashi, Phys. Rev. Lett. **55**, 2676 (1985).

[67] K. Minomo, T. Sumi, M. Kimura, K. Ogata, Y. R. Shimizu, and M. Yahiro, Phys. Rev. Lett. **108**, 052503 (2012).

[68] M. Takechi *et al.*, Phys. Lett. B **707**, 357 (2012).

[69] M. Takechi *et al.*, Phys. Rev. C **90**, 061305(R) (2014).

[70] S. Watanabe, K. Minomo, M. Shimada, S. Tagami, M. Kimura, M. Takechi, M. Fukuda, D. Nishimura, T. Suzuki, T. Matsumoto, Y. R. Shimizu, and M. Yahiro, Phys. Rev. C **89**, 044610 (2014).

[71] Y. Togano *et al.*, Phys. Lett. B **761**, 412 (2016).

[72] T. Nakamura, H. Sakurai, and H. Watanabe, Prog. Part. Nucl. Phys. **97**, 53 (2017).

[73] T. Nagahisa and W. Horiuchi, Phys. Rev. C **97**, 054614 (2018).

[74] S. Bagchi, R. Kanungo, Y. K. Tanaka, H. Geissel, P. Doornenbal, W. Horiuchi, G. Hagen, T. Suzuki, N. Tsunoda, D. S. Ahn, H. Baba, K. Behr, F. Browne, S. Chen, M. L. Cortes, A. Estrade, N. Fukuda, M. Holl, K. Itahashi, N. Iwasa *et al.*, Phys. Rev. Lett. **124**, 222504 (2020).

[75] S. Tagami, M. Tanaka, M. Takechi, M. Fukuda, and M. Yahiro, Phys. Rev. C **101**, 014620 (2020).

[76] W. Horiuchi and T. Inakura, Phys. Rev. C **101**, 061301(R) (2020).

[77] M. Takechi, T. Wakasa, S. Tagami, J. Matsui, and M. Yahiro, Results in Phys. **31**, 104923 (2021).

[78] M. Tanaka *et al.*, Acta Phys. Pol. B **48**, 461 (2017).

[79] Y. Kanada-En'yo, Phys. Rev. C **91**, 014315 (2015).

[80] C. Zeitlin, S. B. Guetersloh, L. H. Heilbronn, A. Fukumura, Y. Iwata, J. Miller, and T. Murakami, Nucl. Phys. A **784**, 341 (2007).

[81] F. Flesch, G. Iancu, W. Heinrich, and H. Yasuda, Rad. Meas. **34**, 237 (2001).